

Global Correlations of Ocean Ridge Basalt Chemistry with Axial Depth and Crustal Thickness

EMILY M. KLEIN AND CHARLES H. LANGMUIR

*Lamont-Doherty Geological Observatory and Department of Geological Sciences
of Columbia University, Palisades, New York*

Regional averages of the major element chemistry of ocean ridge basalts, corrected for low-pressure fractionation, correlate with regional averages of axial depth for the global system of ocean ridges, including hot spots, cold spots, and back arc basins, as well as "normal" ocean ridges. Quantitative consideration of the variations of each major element during melting of the mantle suggests that the global major element variations can be accounted for by ~8-20% melting of the mantle at associated mean pressures of 5-16 kbar. The lowest extents of melting occur at shallowest depths in the mantle and are associated with the deepest ocean ridges. Calculated mean primary magmas show a range in composition from 10 to 15 wt % MgO, and the primary magma compositions correlate with depth. Data for Sm, Yb, Sc, and Ni are consistent with the major elements, but highly incompatible elements show more complicated behavior. In addition, some hot spots have anomalous chemistry, suggesting major element heterogeneity. Thermal modeling of mantle ascending adiabatically beneath the ridge is consistent with the chemical data and melting calculations, provided the melt is tapped from throughout the ascending mantle column. The thermal modeling independently predicts the observed relationships among basalt chemistry, ridge depth, and crustal thickness resulting from temperature variations in the mantle. Beneath the shallowest and deepest ridge axes, temperature differences of approximately 250°C in the subsolidus mantle are required to account for the global systematics.

INTRODUCTION

The temperature and flow regime of the mantle should, in part, control the extent of partial melting that the mantle undergoes as it ascends beneath ocean ridges. The extent of melting should, in turn, govern both the chemistry of ocean ridge basalts and the thickness of the oceanic crust. Crustal thickness, to first order, should be related through isostatic compensation to the zero-age depth of ocean ridges. Thus, variations in ocean ridge basalt chemistry, axial depth, and crustal thickness should correlate with each other and with mantle temperature variations.

Despite the clear conceptual relationship among these parameters, no global correlations between basalt chemistry and axial depth or crustal thickness have yet been established. Petrologists and geochemists have examined certain aspects of this problem, however, on a regional basis. The basic concept of axial "hot spots," which represent one end-member in the global bathymetric spectrum, is related to increased mantle temperature, voluminous magmatism, shallow depths, and greater crustal thickness. In extensive studies of chemical variations along the northern Mid-Atlantic Ridge, *Schilling et al.* [1983] and *Hamelin et al.* [1984] observed that maxima in La/Sm and radiogenic strontium near Iceland and the Azores platform correlate positively with residual depth anomalies and crustal thickness. Furthermore, recent studies of oceanic ultramafic rocks, which are believed to represent the residues of partial melting, have shown correlations between the degree of chemical depletion in basaltic constituents and residual depth [*Michael and Bonatti*, 1985] or residual geoid height [*Dick et al.*, 1984], particularly around the Azores hot spot in the Atlantic. On the opposite bathymetric extreme, we have recently completed a study of basalts erupted in the Australian-Antarctic Discordance, a region of anomalously

great depth and negative gravity anomalies [*Weissel and Hayes*, 1974; *Hayes and Conolly*, 1972]. Comparison of the chemistry of basalts erupted in this "cold spot" with those from normal, as well as hot spot regions, led to a recognition that some chemical parameters vary systematically with axial depth, even in the absence of hot spot anomalies.

In the present study we have examined global systematics in basalt composition and focused on the relationship between chemistry and axial depth. Detailed studies of densely sampled ridge segments have shown considerable small-scale variability in basalt composition, suggesting locally complex petrogenetic histories. In order to identify global chemical systematics, these local variations must be averaged out. We have therefore used data averaged over distances larger than presumed spreading cells.

The identification of global chemical trends requires an extensive, high-quality, global chemical data set. It has only been in the past few years, particularly through the efforts of W. Melson and J.-G. Schilling, that sufficient analyses have been reported on fresh samples recovered from the global system of spreading centers to permit a global synthesis such as that presented here.

DATA TREATMENT AND COMPILATION

Correction for Low-Pressure Fractionation

Probably all ocean ridge basalts have undergone some shallow-level fractionation in crustal magma chambers or conduits, during which the abundances of all major elements are modified from those of their parental magmas. It is the major element contents of the parental magmas, however, that reflect the pressure, temperature, and composition of the mantle from which they are derived. A necessary first step, therefore, is to correct for the effects of shallow-level fractionation.

Two approaches can be used to infer the major element chemistry of parental magmas from a suite of variably fractionated basalts. The first is to consider only

Copyright 1987 by the American Geophysical Union.

Paper number 6B6054.
0148-0227/87/006B-6054\$05.00

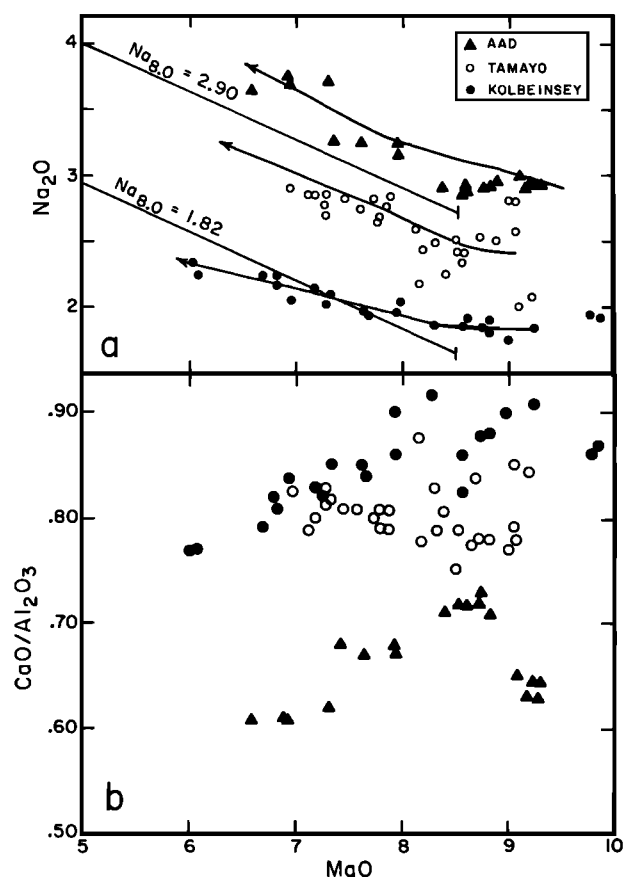


Fig. 1. MgO (wt %) versus (a) Na₂O (wt %) and (b) CaO/Al₂O₃ for basalts from the Kolbeinsey Rise (solid circles) [Schilling *et al.*, 1983], the East Pacific Rise south of the Tamayo transform fault (open circles) [Bender *et al.*, 1984; C.H. Langmuir and J.F. Bender, unpublished data, 1987], and the Southeast Indian Ridge in the vicinity of the Australian-Antarctic Discordance (solid triangles) [Klein *et al.*, 1984]. Arrows in Figure 1a show liquid lines of descent for low-pressure fractionation for each suite, calculated according to the method of Weaver and Langmuir [1987]; also shown are two lines of constant Na_{8.0} the calculated Na₂O contents at 8.0 wt % MgO, as discussed in the text; the formula for calculating Na_{8.0} is given in the caption to Figure 2.

compositions with high MgO contents, which are likely to have experienced fractionation only of olivine. The number of ridge segments that can be studied through this approach, however, is limited; only evolved basalts have been recovered from many regions. The primary approach used in this paper is to correct individual oxide abundances in suites of multiply saturated basalts to a comparable level of MgO in order to compare their chemistries. In addition, for some major or trace element ratios that exhibit little variation during fractionation, arrays of data over a specified range in MgO content have been used. We have also examined the more limited data on lavas of high MgO content to ensure that our conclusions are not an artifact of the correction method.

The approach used to correct for fractionation is illustrated in Figure 1a, which shows data from three areas encompassing much of the range of axial depth displayed by global spreading centers. Although each of these areas is petrologically complex in its own right and probably includes more than one distinct parental magma, data from each area define an array which at any one MgO content is distinct from those of the other areas. Liquid lines of

descent calculated for low-pressure (1 atm) fractionation of olivine, plagioclase, and clinopyroxene from a high MgO magma from each area [Weaver and Langmuir, 1987] pass through the data array for that area. Because the three liquid lines of descent are subparallel, differences in the Na₂O abundances at the same MgO should, to first order, be due to differences in the Na₂O contents of their parental magmas. By projecting along a line parallel to the liquid line of descent when MgO is less than 8.5 wt %, the Na₂O content at some reference value of MgO can be inferred. We have arbitrarily selected 8 wt % MgO as the reference value. The formula used to calculate the Na₂O content at 8 wt % MgO (Na_{8.0}) is given in the caption to Figure 2. Note that a value of Na_{8.0} can be determined for each and every sample with MgO between 5 and 8.5 wt % MgO. For two of the suites, the values of Na_{8.0} calculated for all samples with MgO less than 8.5 wt % agree closely with the actual abundance of Na₂O in a sample with 8 wt % MgO from each suite. For the lowest Na₂O suite, the liquid line of descent has a flatter slope, leading to errors as high as 0.3 in Na_{8.0} for individual points with the lowest MgO; this represents, however, an extreme example of inaccuracy in the correction. Using this technique for fractionation correction, which is essentially the same as that of Langmuir and Bender [1984], even a small number of analyses with MgO less than 8.5 wt % can be used to define a characteristic Na_{8.0} value. Analogous reasoning can be applied to FeO as well, leading to calculated values of Fe_{8.0}. The formula used to calculate Fe_{8.0} is also given in the caption to Figure 2.

Figure 1b shows the variations in the CaO/Al₂O₃ ratios for the same samples. The CaO/Al₂O₃ ratio increases slightly during olivine-plagioclase fractionation but then does not change substantially during fractionation of the three-phase assemblage olivine-plagioclase-clinopyroxene. The decreasing trend of CaO/Al₂O₃ for the Kolbeinsey Ridge data may reflect fractionation at higher pressure where clinopyroxene may be a liquidus phase [e.g., Presnall and O'Donnell, 1976; Bender *et al.*, 1978; Dungan and Rhodes, 1978]. The CaO/Al₂O₃ data from the Australian-Antarctic Discordance show substantial variation, which is also reflected in the trace element chemistry from this region, but samples from a single dredge approximately follow the low-pressure fractionation trend. Despite the complexities in the data and fractionation histories, the three regions are distinguishable in their CaO/Al₂O₃ ratios, which correlate inversely with Na_{8.0}. Thus for a variety of chemical parameters, it is possible to "see through" both low pressure fractionation and local complexities to obtain a regional geochemical signature.

Data

Regional averages of smoothed axial depth, Na_{8.0}, Fe_{8.0} and CaO/Al₂O₃ in basaltic glasses and whole rocks are presented in Table 1. References for the sources of the data, the number of analyses included in each average, and the standard deviations for each average are also reported. The CaO/Al₂O₃ ratios were calculated for samples with greater than 5 wt % MgO, and the Na_{8.0} and Fe_{8.0} values were calculated for samples with MgO contents between 5 and 8.5 wt %. For regions where only whole rock data were available and where information on the extent of whole rock alteration was given, analyses of highly altered samples were excluded from our computations.

Because sampling density varies considerably from ridge to ridge, some spreading centers, such as the northern Mid-Atlantic Ridge (MAR) or portions of the East Pacific Rise (EPR), are better represented than other, more sparsely sampled spreading centers, such as the Southwest or Southeast Indian Ridges. The chemical data were averaged as follows. For ridges where sampling density was high, samples were grouped with respect to the tectonic segmentation of the ridge axis, and regional averages were calculated for all samples within each ridge segment. Thus, for the densely sampled and tectonically complex Easter microplate region, the EPR was divided into seven segments based largely upon transform-bounded segmentation of the ridge axes. Similarly, in the densely sampled region just south of the Kane Fracture Zone along the MAR, a small ridge offset was selected as a boundary between ridge segments. For densely sampled spreading centers, analyses were thus generally averaged over less than 100 km of ridge length. In contrast, for the numerous spreading centers where sampling density is sparse, averages were taken of all available data from a particular region, which may encompass a few hundred kilometers of ridge length. No average is reported for regions where only one analysis is available over distances of a few hundred kilometers.

Most of the chemical data are from four laboratories: W. Melson's and H. Sigurdsson's microprobe analyses of basaltic glasses, J.-G. Schilling's analyses of basaltic whole rocks, and our own analyses of hand-picked glass powders by plasma spectrometry. Our comparison of analyses by the four laboratories suggests that there are systematic interlaboratory biases, particularly for MgO, Na₂O, and TiO₂. These biases, however, are small compared to the range of regional chemical variations presented herein. The analyses from Melson's microprobe are from areas that span the entire bathymetric range, and therefore chemical correlations with depth cannot be attributed to interlaboratory biases.

Standard deviations for all regional averages of Na₂O, Fe₂O₃ and CaO/Al₂O₃ are reported in Table 1. For the vast majority of averages, the standard deviations are less than 5–10% of the total range of the data which shows that the global systematics are not an artifact of the averaging process. A small number of regional averages, particularly in the vicinity of recognized hot spots, exhibit larger standard deviations.

Regional axial depth values reported in Table 1 represent our best estimate of the average over the range of bathymetric data published for a particular region. References for the bathymetric data from which our estimates were made are included in the footnotes of Table 1. In determining the regional depth values for regions of good bathymetric coverage, we have been guided by the work of *Le Douarin and Francheteau* [1981], who determined a smoothed axial depth profile for the northern MAR by taking moving averages with a 100 km step. Qualitatively, our value for regional axial depth would represent the mean depth of such a smoothed profile over the ridge length in question. For a few regions, however, the reported bathymetric data are limited, and in such cases, we have simply used the mean of the axial depth information that is available in published papers. It should be noted that for the purposes of examining global correlations between axial depth and chemistry, an error of as much as a few hundred

meters in axial depth is small compared to the total global spreading center bathymetric range of 5600 m.

RESULTS

Correlations Between Chemistry and Axial Depth

Regional averages of Na₂O, CaO/Al₂O₃, and Fe₂O₃ are plotted versus regional averages of axial depth in Figures 2a–2c. The data include normal mid-ocean ridge basalts (MORB) from the Atlantic, Pacific, and Indian ocean ridges, enriched MORB from axial hot spots (such as Iceland, the Azores, Easter microplate, and the Galapagos), basalts erupted in back arc basins, and basalts erupted in such tectonically unique settings as the Cayman Trough and Woodlark basin. There is a clear positive correlation between Na₂O and depth (Figure 2a). The regional averages of CaO/Al₂O₃ and Fe₂O₃ correlate inversely with axial depth for all basalts, with the exception of some axial hot spots; some hot spots, in particular the Azores, Jan Mayen, and Galapagos regions, show lower CaO/Al₂O₃ and Fe₂O₃ than other basalts erupted at the same depth (Figures 2b and 2c).

Within the overall correlations there are areas with different local systematics. For example, averages taken over the topographically highest ridge segments associated with Atlantic and Pacific hot spot centers (Figure 2a) tend to have higher Na₂O, for the same depth (or are shallower for the same Na₂O), and therefore the data for most hot spot centers skirt the upper boundary of the broad band defining the global correlation. Much of the lower boundary of the correlation is formed of samples from the margins of hot spots, that is, the bathymetrically deeper regions on the peripheries of hot spots. This can lead to the opposite correlation between Na₂O and depth for these hot spot areas when any one of them is considered in isolation. Around the Galapagos hot spot, for example, all data fall within the broad, positive, global correlation band (Figure 2a), yet five of the seven ridge segments define an inverse trend within this band.

The trends of opposite slope observed around hot spots apparently reflect processes occurring at shorter wavelengths than the overall correlation. Figure 2d shows the data from Table 1 averaged over >500 km of ridge length, using major tectonic boundaries as delimiting points. Over these longer ridge lengths, the variations within each hot spot region are averaged, the correlation becomes more clearly defined and distinctly curvilinear, and different ocean basins form distinct fields. This suggests that the differences in Na₂O between hot spot centers and margins is a medium-wavelength perturbation on the processes that govern the global correlation between depth and Na₂O.

The width of the global Na₂O–depth correlation (up to ~1500 m in depth or 0.6 in Na₂O) is substantial and clearly indicates the existence of multiple causes of variation in depth and chemistry, even when short-wavelength variations are averaged out. In this paper, however, we concentrate on the cause only of the overall global trends of the data because these trends should reflect first-order causes of MORB variations on a global scale.

Comparison With Previous Chemistry/Depth Correlations

There have been several previous papers which have shown relationships between chemistry and depth for oceanic basalts. All of these previous efforts have been

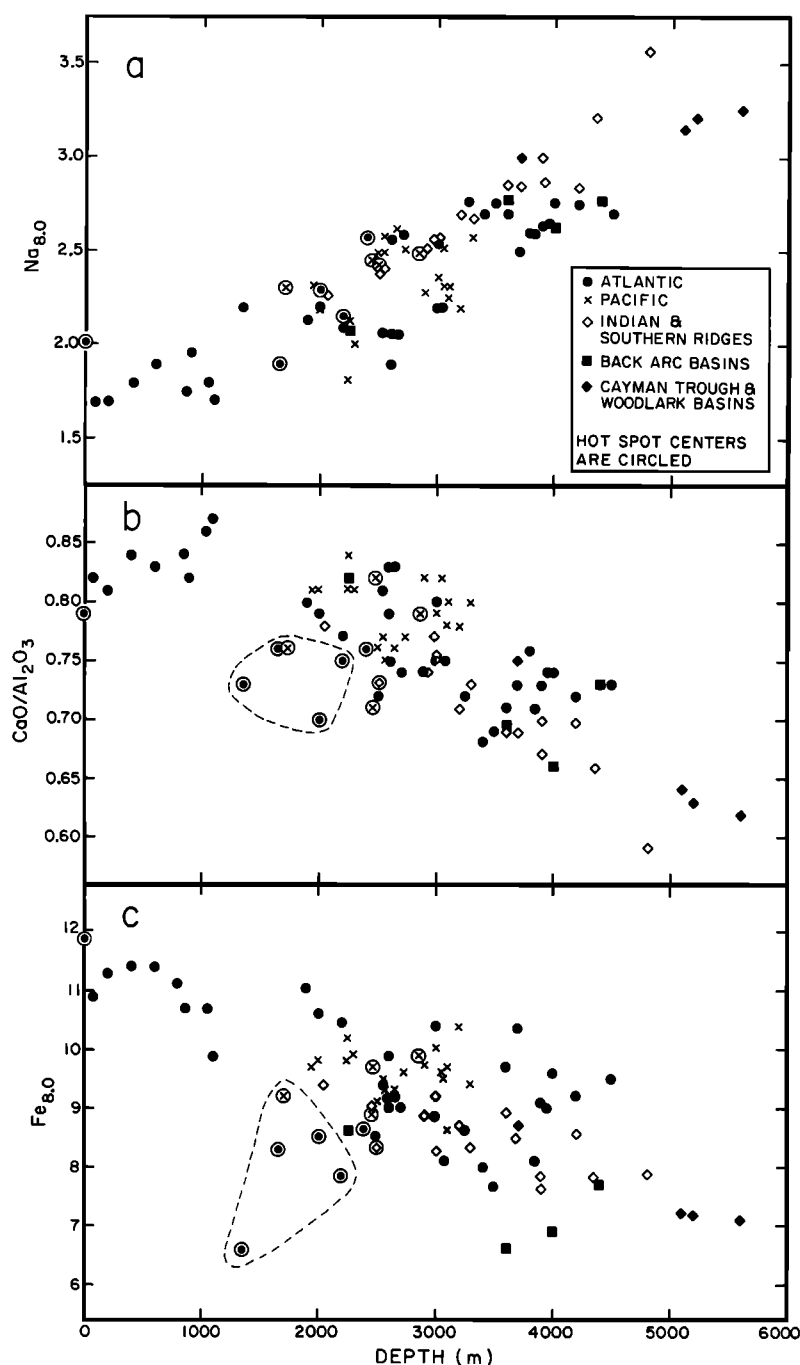


Fig. 2. Regional averages of axial depth versus (a) $\text{Na}_{8.0}$ (b) $\text{CaO}/\text{Al}_2\text{O}_3$, and (c) $\text{Fe}_{8.0}$ for samples from the Mid-Atlantic Ridge (solid circles), Pacific ridges (crosses), Indian and southern ridges (open diamonds), back arc basins (solid squares), and the Mid-Cayman Rise and Woodlark basin (solid diamonds); recognized axial hot spot centers are circled. Data and references are given in Table 1. Data points from the Azores, Jan Mayen and Galapagos hot spot centers which are anomalous on Figures 2b and 2c are enclosed in a dashed field. (d) Long-wavelength $\text{Na}_{8.0}$ versus axial depth; data from Table 1 have been combined and, where sampling density permitted, averaged over >500 km of ridge length; in particular, hot spot centers and margins have been averaged together. $\text{Na}_{8.0} = \text{Na}_2\text{O} + 0.373 \cdot (\text{MgO}) - 2.98$; $\text{Fe}_{8.0} = \text{FeO} + 1.664 \cdot (\text{MgO}) - 13.313$. $\text{Na}_{8.0}$ and $\text{Fe}_{8.0}$ are calculated for samples with 5.0–8.5 wt % MgO; $\text{CaO}/\text{Al}_2\text{O}_3$ are calculated for samples with >5.0 wt % MgO.

restricted in coverage, however, and the results presented herein differ in several fundamental ways.

The most well-known relationship between chemistry and depth is the decrease in incompatible element abundance and La/Sm with increasing distance from Iceland (and hence increasing depth) along the Reykjanes Ridge, first established by Schilling [1972]. It has since been shown

that for many hot spots near ridges there is a fairly regular change in La/Sm and radiogenic isotope ratios with increasing distance from the hot spot, and therefore with increasing depth [e.g., Schilling *et al.*, 1982, 1983, 1985; Sun *et al.*, 1975; Hart *et al.*, 1973; Verma and Schilling, 1982]. Hamelin *et al.* [1984] proposed an overall correspondence between depth and Pb and Sr isotopic

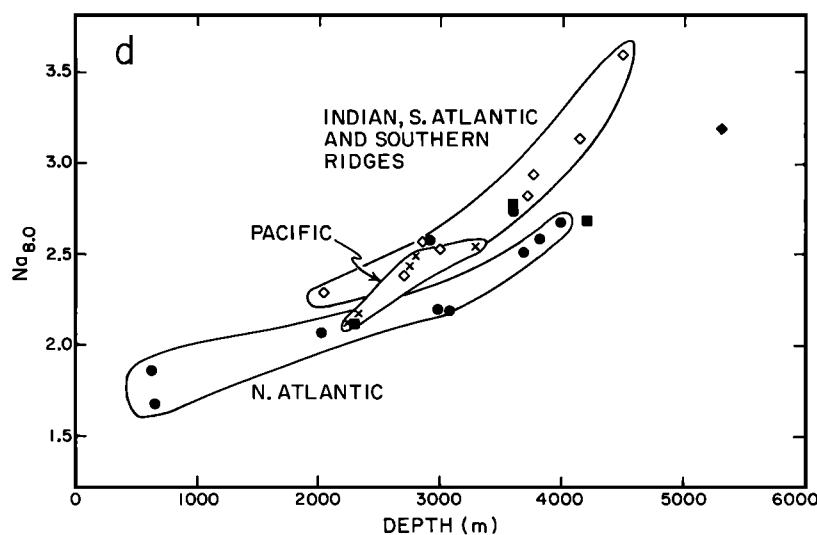


Fig. 2. (continued)

composition for the North Atlantic, although the slope of the correlation is different for each hot spot.

There are two important distinctions between the global correlations of Figure 2 and the previous results from around hot spots. First, the previous correlations were based primarily on incompatible trace elements and radiogenic isotopes and not on major elements. Second, all of the previous correlations between depth and incompatible element or isotopic composition apply only to individual hot spots and do not apply globally. For example, the MAR near the Azores platform is much deeper than is Iceland, yet the La/Sm and $^{87}\text{Sr}/^{86}\text{Sr}$ ratios near the Azores are much higher. Indeed, one of the major points made by Schilling *et al.* [1983] was the contrast in chemistry between the Azores and Iceland regions. But such contrasts are not restricted to hotspots. Sr isotopic data for some basalts from the Australian-Antarctic Discordance are similar to those reported from Iceland, yet the two regions represent extremes in both $\text{Na}_{8.0}$ and bathymetry [Klein *et al.*, 1984; Schilling *et al.*, 1983].

Furthermore, we noted above the contrast between local $\text{Na}_{8.0}$ -depth variations around some individual hot spots and the overall global correlation. If the hot spot signature dominated the global correlation between depth and $\text{Na}_{8.0}$ then one might expect a negative global correlation of $\text{Na}_{8.0}$ and depth, since shallow hot spot centers tend to be higher in $\text{Na}_{8.0}$ than the deeper margins of hot spots. Thus there are fundamental distinctions between the previously noted correlations around hot spots and the global correlations presented in Figure 2.

Michael and Bonatti [1985] have recently shown a correlation between the composition of minerals from ultramafic rocks recovered from the North Atlantic and depth of the ridge axis. In addition, Dick *et al.* [1984] showed correlations between the chemistry of abyssal ultramafic rocks and both residual geoid and the chemistry of spatially associated basalts for several localities in the Atlantic and Indian oceans. The combination of these observations leads to a result that is completely consistent with the global regularities of Figure 2. In view of the paucity of the abyssal ultramafic data base and the inherent ambiguities in the representativeness of small ultramafic samples, it is

remarkable that these studies captured the essence of the global regularities illustrated in Figure 2. We note, however, that the results of Michael and Bonatti [1985] and Dick *et al.* [1984] were dominated by data from the central North Atlantic. In the global correlations of Figure 2 it appears that the central North Atlantic region may be in fact chemically anomalous in a global context.

POSSIBLE CAUSES OF THE GLOBAL CORRELATIONS

The fact that regional averages from all spreading centers, with the exception of some hot spot centers, define correlations between $\text{Na}_{8.0}$, $\text{CaO}/\text{Al}_2\text{O}_3$, $\text{Fe}_{8.0}$, and depth (Figure 2) suggests that there are processes that govern both axial depth and aspects of basalt chemistry on a global scale, despite the complicated petrogenetic histories of local areas. In the following, we consider three possible explanations for the observed correlations: clinopyroxene fractionation, major element source heterogeneity, and varying extents of partial melting. Although there is evidence for the importance of all of these to some extent in various areas, the partial melting model alone provides a straightforward explanation of the first-order correlation between regional basalt chemistry and average depth.

Much of the discussion that follows in this section involves detailed geochemical modeling and comparison of the global data to the results of experimental studies on the melting behavior of periodites. The key point is that the overall global systematics are consistent with varying extents of melting at varying pressures, with basalts from the shallowest ridge segments produced by larger extents of melting deeper in the mantle. The implications of these conclusions are explored in the discussion section.

Clinopyroxene Fractionation

Sodium behaves as a moderately incompatible element with respect to clinopyroxene and the $\text{CaO}/\text{Al}_2\text{O}_3$ ratio in clinopyroxene is high [e.g., Dungan and Rhodes, 1978]. Thus substantial clinopyroxene fractionation would be expected to produce an inverse correlation between $\text{CaO}/\text{Al}_2\text{O}_3$ and $\text{Na}_{8.0}$ similar to that observed.

The total variation in regional $\text{CaO}/\text{Al}_2\text{O}_3$ is 0.59-0.87. Typical low-pressure clinopyroxenes contain about 20 wt %

TABLE 1. Regional Averages of Smoothed Axial Depth and Parameters of Basalt Chemistry for Oceanic Spreading Centers

Region	Latitude or Longitude, deg	Smoothed Axial Depth, km	Na ₂ O	s.d.	Fe ₂ O ₃	s.d.	N	CaO/ Al ₂ O ₃	s.d.	N	Reference
<i>Ocean Ridges</i>											
North Atlantic	75.52-77.53N	3500	2.74	0.52	7.64	0.74	10	0.69	0.02	13	1,2
	73.74-74.69N	3250	2.75	0.11	8.61	0.89	7	0.72	0.02	8	1,2
	72.61-73.52N	3000	2.53	0.25	8.85	0.92	12	0.75	0.03	19	1,2
	71.53-72.32N	2500	2.43	0.21	8.55	1.17	16	0.72	0.05	19	1,2
	71.24-71.43N	2200	2.14	0.08	7.82	1.16	3	0.75	0.05	5	1,2
	69.15-70.66N	1050	1.84	0.10	10.71	0.58	4	0.86	0.03	7	1,3
	66.51-68.63N	400	1.77	0.15	11.41	0.68	10	0.84	0.05	17	1,3
	63.85-64.79N	0	1.98	0.16	11.91	0.64	10	0.79	0.04	18	1,3
	62.99-63.57N	200	1.68	0.15	11.25	0.64	14	0.81	0.04	14	1,3
	60.73-62.90N	600	1.93	0.09	11.37	0.45	14	0.83	0.02	17	1,3
	59.99-60.45N	900	1.96	0.08	11.14	0.27	6	0.82	0.02	6	1,3
	57.14-58.87N	1900	2.12	0.11	11.04	0.63	3	0.80	0.04	4	1,3,4
	53.41-55.67N	2200	2.09	0.07	10.45	0.46	4	0.77	0.04	4	1,3,4
	50.04-52.01N	3825	2.59	0.19	8.12	1.36	4	0.71	0.02	5	1,3
	42.79-46.23N	3075	2.19	0.30	8.09	1.38	4	0.75	0.03	11	1,3
	39.76-40.23N	2600	1.90	0.09	9.04	0.78	5	0.79	0.02	6	5,3
	39.63N	2000	2.33	0.46	8.49	1.26	4	0.70	0.06	6	5,3
	38.70-39.20N	1350	2.20	0.19	6.59	0.76	3	0.73	0.07	3	5,3
	37.73N	1650	1.88	0.06	8.30	0.08	3	0.76	0.02	3	5,3
	35.84-36.77N	2550	2.08	0.10	9.41	0.47	10	0.81	0.02	12	5,3
	34.23N	3000	2.17	0.12	10.40	0.56	3	0.80	0.02	3	5,3
	29.07-32.62N	3700	2.51	0.13	10.37	0.58	5	0.73	0.03	7	5,3
	70.17-70.93N	1100	1.67	0.09	9.85	0.82	3	0.87	0.03	4	1,6*
	63.29-63.64N	75	1.67	0.20	10.88	0.45	11	0.82	0.03	11	1,6*
	59.75-61.99N	850	1.74	0.06	10.71	0.17	6	0.84	0.03	6	1,6*
	52.99-53.19N	2000	2.20	0.13	10.57	0.39	5	0.79	0.04	6	1,6*
	36.64-36.83N	2650	2.05	0.17	9.21	0.35	55	0.83	0.03	56	7,8*
	36.42-36.49N	2600	2.05	0.13	8.98	0.82	54	0.83	0.03	60	7,8*
	27.20-29.28N	3600	2.68	0.18	9.70	0.82	4	0.71	0.03	8	5,6*
	23.78-24.18N	3800	2.60	0.09	8.18	0.25	4	0.76	0.01	4	9,10,6*
	23.22-23.67N	4200	2.74	0.17	9.19	0.52	16	0.72	0.03	16	9,10,6*
	22.17-22.52N	3900	2.64	0.14	9.11	0.33	11	0.73	0.04	11	5,6*
	18.92-21.09N	3950	2.64	0.09	9.00	0.40	4	0.74	0.05	4	5,6*
	11.40-11.97N	4500	2.70	0.10	9.46	0.50	5	0.73	0.03	5	5,6*
South Atlantic	22.92-21.87S	4000	2.75	0.21	9.60	0.76	6	0.74	0.03	6	11,6*
	34.55S	2700	2.58	0.03	8.98	0.49	2	0.74	0.00	2	12
	35.28S	3400	2.68	0.14	7.99	0.35	2	0.68	0.01	2	12
	36.07-37.83S	2400	2.57	0.09	8.63	0.53	6	0.76	0.02	6	12
American-Antarctic	40.44-42.92S	2600	2.67	0.16	9.89	0.61	3	0.75	0.01	3	12
	17.97-18.06W	3900	2.88	0.30	7.83	0.22	3	0.70	0.07	3	13,6*
	16.21-16.32W	4350	3.21	0.10	7.81	0.48	4	0.66	0.02	4	13,6*
	7.01-7.66W	4200	2.84	0.16	8.57	0.69	7	0.70	0.03	7	13,6*
Southwest Indian	6.04-6.06W	3700	2.84	0.13	8.40	0.81	7	0.69	0.04	8	13,6*
	4.45-4.70W	3300	2.68	0.07	8.32	0.40	2	0.73	0.01	2	13,6*
	53.99-54.37S	2500	2.38	0.22	8.34	0.91	9	0.73	0.05	10	14,6*
	28.85-26.62S	4800	3.58	0.27	7.93	0.82	5	0.59	0.02	6	15,6,16*
Central Indian	24.98-20.15S	2900	2.52	0.27	8.94	0.21	4	0.74	0.04	5	15,6*
	19.83-18.71S	2500	2.37	0.12	9.02	0.56	2	0.75	0.06	2	17,6*
	15.55-12.42S	3000	2.55	0.18	8.24	0.67	3	0.75	0.03	3	17,6*
Carlsberg	5.05- 5.36N	3200	2.68	0.11	8.67	1.22	7	0.71	0.03	7	18,6*
Red Sea	21.35-25.00N	2050	2.28	0.12	9.41	1.36	10	0.78	0.03	12	19,6*
Southeast Indian	115.38-119.18E	3600	2.86	0.23	8.86	0.66	26	0.69	0.04	26	20,21*
	121.03-127.08E	3900	3.00	0.22	7.56	1.03	27	0.67	0.05	27	20,21*
	130.05-137.56E	2975	2.55	0.30	9.19	0.37	34	0.77	0.06	34	20,21*
Juan de Fuca	44.75N	2250	2.12	0.07	10.20	0.10	4	0.84	0.00	4	22,23*
Gorda	41.50-42.80N	3300	2.56	0.09	9.44	0.43	7	0.80	0.03	7	23*
East Pacific Rise	22.83-22.95N	3100	2.31	0.09	9.68	0.25	10	0.80	0.02	10	24,25*
	22.35-22.70N	2900	2.28	0.15	9.74	0.43	15	0.82	0.03	18	24,25*
	12.47-14.28N	2650	2.60	0.15	9.31	0.49	48	0.76	0.03	52	26,25
	10.29-11.51N	2570	2.47	0.14	9.31	0.56	21	0.75	0.04	21	26,25
	8.62-10.21N	2550	2.57	0.11	9.45	0.70	8	0.77	0.03	8	26,25
	5.63- 8.40N	2730	2.50	0.14	9.56	0.40	11	0.77	0.02	11	38,25
Galapagos Spreading Center	86.30-87.48W	2250	1.82	0.09	9.76	0.83	7	0.81	0.02	8	27,28
	87.86-89.59W	2000	2.19	0.11	9.79	1.07	8	0.81	0.04	8	27,28
	89.99-91.26W	1700	2.32	0.28	9.23	1.01	12	0.76	0.05	12	27,28
	91.61-92.90W	1950	2.33	0.22	9.68	0.35	5	0.81	0.03	5	27,28

TABLE 1. (continued)

Region	Latitude or Longitude, deg	Smoothed Axial Depth, km	Na ₂ O	s.d.	FeO	s.d.	N	CaO/ Al ₂ O ₃	s.d.	N	Reference
Easter Microplate Eastern Ridge	93.34-94.45W	2300	2.03	0.03	9.89	0.56	6	0.81	0.03	6	27,28
	94.87-95.62W	3200	2.17	0.07	10.43	1.05	3	0.78	0.04	4	27,28
	96.18-99.56W	3100	2.24	0.10	8.55	0.56	5	0.78	0.03	5	27,28
	27.21-29.02S	2500	2.48	0.33	9.10	0.50	7	0.76	0.05	7	29,30
	25.98-26.92S	2450	2.44	0.11	8.86	0.49	6	0.71	0.06	6	29,30
	24.86-25.66S	3060	2.29	0.61	9.46	0.37	5	0.75	0.04	5	29,30
	23.54-24.78S	3050	2.52	0.42	9.56	0.82	5	0.82	0.03	5	29,30
	24.64-26.70S	2480	2.43	0.16	9.72	0.19	7	0.82	0.02	7	29,30
	23.25-24.31S	2850	2.48	0.20	9.89	0.56	4	0.79	0.03	4	29,30
	22.53-23.08S	3000	2.36	0.11	9.97	0.62	4	0.79	0.04	4	29,30
<i>Back Arc Basins</i>											
Marianas Trough	17.39N	4000	2.63	0.04	6.86	1.38	6	0.66	0.05	7	31,6,32*
	18.01N	4400	2.77	0.44	7.72	1.34	3	0.73	0.07	3	31,6,32*
Lau Basin	15.17-18.76S	2250	2.09	0.31	8.59	1.57	9	0.82	0.06	9	33,6,32*
Scotia Sea	56.40-60.07S	3600	2.77	0.07	6.57	0.12	5	0.69	0.01	5	34,6,32*
<i>Other Spreading Centers</i>											
Cayman Trough	18.36-18.61N	5200	3.21	0.10	7.17	0.78	5	0.63	0.01	5	35,6,36*
	18.09-18.13N	5600	3.25	0.14	7.10	0.45	10	0.62	0.01	11	35,6,36*
	17.98-18.07N	5100	3.16	0.16	7.23	0.72	10	0.64	0.01	10	35,6,36*
Woodlark Basin	9.09-9.50N	3700	2.96	0.19	8.71	0.23	18	0.75	0.03	18	37

Na₂O and FeO are calculated values of Na₂O and FeO at 8 wt % MgO, as discussed in the text and caption to Figure 2; s.d. refers to one standard deviation. *N* is the number of samples used to compute each mean. Reference column indicates reference numbers for the sources of the bathymetric and chemical data, as indicated below; where only one number is given, chemical and bathymetric data are from the same reference. Smoothed axial depth refers to average depth to neovolcanic zone.

* Data from these references are included in a 1981 version of the Smithsonian Institution catalog of basalt glasses; see reference 6.

The majority of the chemical data from the North Atlantic are either from Schilling *et al.* [1983] or W. Melson (see reference 6); both sets of data were used in order to achieve the fullest possible coverage; for a few North Atlantic ridge segments, there is overlap between the two data sets.

References: 1, Vogt [1986]; 2, Neumann and Schilling [1984]; 3, Schilling *et al.* [1983]; 4, Lamont-Doherty Geological Observatory (L-DGO) unpublished plasma analyses; 5, Le Douarin and Francheteau, [1981]; 6, 1981 version of the Smithsonian Institution catalog of basalt glass analyses, which includes analyses reported by Melson *et al.* [1976, 1977] and Melson and O'Hearn [1979, 1986]; 7, Phillips and Fleming [1978]; 8, Stakes *et al.* [1984]; 9, Pockalny *et al.* [1985]; 10, Bryan *et al.* [1981]; 11, N. Cherkis (personal communication, 1987); 12, Humphris *et al.* [1985]; 13, Lawver and Dick [1983], samples of leRoex *et al.* [1985]; 14, Sclater *et al.* [1976]; 15, Sclater *et al.* [1981]; 16, Price *et al.* [1986]; 17, Fisher *et al.* [1971]; 18, McKenzie and Sclater [1971]; 19, Bonatti *et al.* [1984]; 20, Weissel and Hayes [1974]; 21, E. Klein *et al.* (manuscript in preparation, 1987); 22, Kappel and Ryan [1986]; 23, E. Kappel (unpublished data, 1986); 24, Tamayo Scientific Team [1984]; 25, L-DGO, unpublished analyses: samples from 5-14°N of Langmuir *et al.* [1986]; 26, Macdonald *et al.* [1984]; 27, Christie and Sinton [1981]; 28, Schilling *et al.* [1982]; 29, Hey *et al.* [1985]; 30, Schilling *et al.* [1985]; 31, Fryer and Hussong [1981]; 32, Fryer *et al.* [1981]; 33, Hawkins [1976]; 34, Barker [1972]; 35, Stroup and Fox [1981]; 36, Thompson *et al.* [1980]; 37, Perfit *et al.* [1987]; 38, Klugord and Mammerick [1982].

CaO and 4 wt % Al₂O₃ [Shibata *et al.*, 1979; Grove and Bryan, 1983]. Thus, to produce the observed range in CaO/Al₂O₃ would require approximately 25-30% equilibrium crystallization of low-pressure clinopyroxene. This amount of crystallization, however, would increase the Na₂O abundances in the residual liquids by only 30-50%, much less than the factor of 2 variations observed. If high-pressure, aluminous clinopyroxene were the crystallizing phase, more crystallization would be required to produce the observed range in CaO/Al₂O₃ ratios, which might lead to the requisite increase in Na₂O.

However, there are two aspects of the data which are not consistent with high-pressure clinopyroxene fractionation. First, such crystallization would progressively lower MgO;

one would therefore expect the compositions from different areas to converge at high MgO contents, and the observed variations in chemistry to occur only at low values of MgO. In fact, the chemical variations between different regions remain distinct for all extents of fractionation (e.g., Figure 1) and appear to be fundamental features of the parental magmas. Second, because clinopyroxenes have less FeO than the magmas from which they crystallize, clinopyroxene crystallization would lead to progressively higher FeO contents with decreasing CaO/Al₂O₃ and increasing NaO. This is opposite to the observed global trends; areas of high CaO/Al₂O₃ and low Na₂O have the greatest FeO abundances, not the least. Thus, although high-pressure clinopyroxene fractionation may occur, it is not an adequate

explanation for the global correlations. It may, however, cause some of the scatter within the correlations, particularly for Fe_{8.0}.

Varying Source Compositions

A second possible model is that the depth/chemistry systematics result from source heterogeneity in major element composition and hence mineralogy. While it is clear that the mantle is heterogeneous with respect to highly incompatible trace element abundances and isotopic composition [e.g., *Schilling et al.*, 1983], the evidence for major element source heterogeneity on the scale sampled by melting has been more ambiguous [*Langmuir and Hanson*, 1980; *Sigurdsson*, 1981; *Bryan and Dick*, 1982; *Dick et al.*, 1984]. Nevertheless, it is important to explore the possibility that the observed chemical systematics result from major element source heterogeneity. In the simplest model, all samples would be produced by approximately the same extents of melting and the observed chemical variations would reflect the extent of fertility or depletion of the source. Samples produced by melting of a more fertile source, for example, would be expected to have higher Na₂O, Al₂O₃, and FeO than samples produced by the same extent of melting of a more depleted source. This would lead to a positive rather than the observed inverse correlation between Na_{8.0} and Fe_{8.0}.

This simple model will not strictly apply, however, because the more depleted mantle would have a higher solidus temperature and hence would melt less, leading to a relative enrichment in Na₂O. Source depletion is thus compensated for, to some extent, by the decrease in melting. However, for elements with small partition coefficients, such as Na₂O, the effect of source depletion far outweighs that of decreased melting. Hence a simple model of major element heterogeneity predicts a positive rather than the observed inverse correlation between Na_{8.0} and Fe_{8.0}. Major element source heterogeneity may, however, contribute to some of the scatter of Figures 2a-2c.

In particular, two aspects of the data, may require source heterogeneity. First, the >500 km-wavelength chemical averages (Figure 2d) show that the Indian and North Atlantic ridges form distinct curvilinear trends within the overall global correlation. This fine-structure within the overall correlation may result from major element and mineralogical heterogeneities. Second, samples from ridges near the Azores, Jan Mayen, Galapagos and, to a lesser extent, Easter microplate hot spot regions do not plot on the global trends of CaO/Al₂O₃ and Fe_{8.0} versus depth, but show markedly lower values for the same depth compared to other regions (Figures 2b and 2c). *Schilling et al.* [1983] attributed the low CaO/Al₂O₃ ratios and low Sc abundances in the former two areas to enhanced clinopyroxene crystallization. *Langmuir and Hanson* [1980] noted the unusually low FeO content of basalts from the MAR near the Azores and suggested that the low FeO resulted from major element heterogeneity. *Sigurdsson* [1981] observed that both the FeO and SiO₂ contents of these samples were too low to be explained exclusively by clinopyroxene fractionation. Thus the Azores, Jan Mayen, Galapagos, and, to a lesser extent, Easter microplate plumes appear to be anomalous in a global context and may represent evidence of major element source heterogeneity.

Varying Extents of Partial Melting

Melting beneath ridges is likely to occur by adiabatic upwelling of the mantle. In this case, for a given mantle composition, the amount of melt produced should be controlled largely by the temperature of intersection of the mantle solidus. An obvious third model to explore, then, is that the global correlations of Figure 2 reflect different extents of melting in response to variations in the temperature of the mantle. To explore this model, it is necessary to understand how major elements vary in response to differences in the extent and pressure of melting of the mantle.

EVALUATION OF THE PARTIAL MELTING HYPOTHESIS

Major Element Systematics During Partial Melting

A number of experimental studies in recent years [e.g., *Jaques and Green*, 1980; *Fujii and Scarfe*, 1985; *Takahashi*, 1985; *Takahashi and Kushiro*, 1983; *Mysen and Kushiro*, 1977] have provided an adequate data base to infer the response of most major elements to increasing extents of melting. In this section we attempt to synthesize these data to constrain the extents and pressures of melting for the basalt data.

Experimental data show that Na₂O is perfectly incompatible with respect to olivine, strongly incompatible with respect to orthopyroxene, and that at pressures above plagioclase stability (approximately 8-9 kbar [*Presnall et al.*, 1979]) the mantle budget of Na₂O resides primarily in clinopyroxene. For the extents of melting relevant to MORB (see quantitative modeling below), plagioclase stability is expected to play only a minor role in the melting systematics of Na₂O. To a first order, it appears, therefore, that Na₂O behaves as a moderately incompatible trace element, showing highest concentrations at the smallest extents of melting and decreasing in concentration by dilution as the extent of melting increases [*Jaques and Green*, 1980; *Fujii and Scarfe*, 1985]. Therefore, if Na_{8.0} approximates the sodium abundances in relatively primitive magmas and the Na₂O content of the source is constant, variations in the abundances of Na₂O from region to region may indicate variations in the extents of melting. *Dick et al.* [1984] and *Michael and Bonatti* [1985] reached similar conclusions regarding the behavior of Na₂O during melting of the mantle, based on their studies of oceanic peridotites.

CaO and Al₂O₃ also appear to show systematic behavior during melting of spinel lherzolite (Figure 3a). *Fujii and Scarfe* [1985] and *Jaques and Green* [1980] showed that Al₂O₃ abundances are highest in the first increments of melt and decrease with further extents of melting of spinel lherzolite. CaO appears to show somewhat more complicated melting behavior. CaO increases as clinopyroxene melts, but when clinopyroxene is no longer present as a residual phase, CaO decreases with further melting. Thus the CaO/Al₂O₃ ratio shows the following systematics: CaO/Al₂O₃ is at a minimum as melting begins; it increases thereafter until clinopyroxene has melted out, at which point it has a higher value than the initial source because some Al₂O₃ remains in orthopyroxene; as melting proceeds and Al₂O₃ from orthopyroxene is added to the melt, the CaO/Al₂O₃ ratio decreases slightly. It is important to note that as long as clinopyroxene is present

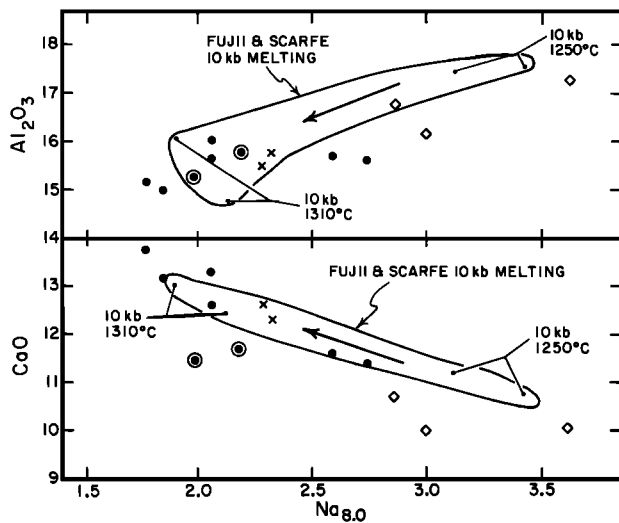


Fig. 3. Na_2O versus Al_2O_3 (wt %) and CaO (wt %) for representative samples with 8.5–10.0 wt % MgO . Symbols are as in Figure 2. Also shown are fields for progressive melting of two synthetic spinel lherzolites at 10 kbar, and the two melt compositions for the reported temperature extremes of 1250°C and 1310°C [from Fujii and Scarfe, 1985]. Arrows indicate direction of compositional change with increasing extents of melting. Na_2O was calculated from the reported analyses after correction to 8.5 wt % MgO by removal of Fe_0 olivine. Note that the trends of the basalt data are sub-parallel to the trends of the experimental melt fields.

as a residual phase, increasing extents of melting cause an increase in the $\text{CaO}/\text{Al}_2\text{O}_3$ ratio. The data of Jaques and Green suggest further that there is a slight pressure dependence to the partitioning of Al_2O_3 during melting; at higher pressure, the solubility of Al_2O_3 in pyroxenes increases, leading to lower Al_2O_3 in coexisting magmas (see Figure 4).

The distribution of FeO and MgO during melting of the mantle has been calculated and discussed in detail by

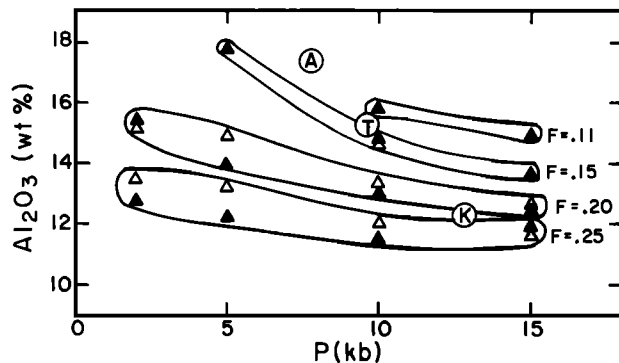


Fig. 4. Al_2O_3 in melts produced by progressive melting of pyrolite (open triangles) or Tinaquillo lherzolite (solid triangles) versus the pressure of melting; data are from Jaques and Green [1980]. F indicates extent of melting for each field; where necessary, melt compositions at the particular extent of melting indicated have been extrapolated from the reported melt intervals. K, T, and A refer to averages for samples from the Kolbeinsy Ridge, EPR south of the Tamayo transform, and the Australian-Antarctic Discordance, respectively, and were plotted according to their Al_2O_3 abundances and inferred extents of melting, back-corrected to primary MgO contents of 15%, 12%, and 10%, respectively, to correspond to Figure 5.

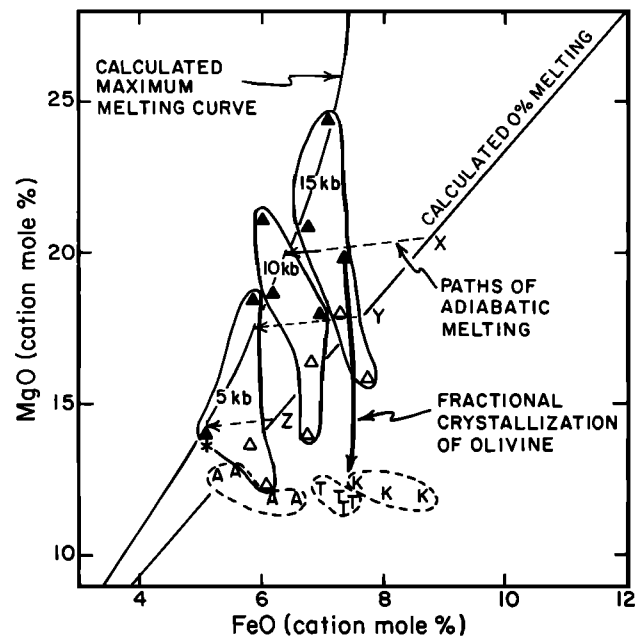


Fig. 5. FeO versus MgO (cation mole percent) [after Langmuir and Hanson, 1980]. The 0% melting line and the maximum melting curve are calculated for an initial bulk composition for pyrolite reported by Jaques and Green [1980]. Also shown are melt compositions produced by progressive melting of pyrolite (open triangles) and Tinaquillo lherzolite (solid triangles) at pressures of 5, 10, and 15 kbar, reported by Jaques and Green [1980]. The star indicates a melt composition produced by melting of natural spinel lherzolite at 10 kbar, reported by Takahashi [1985]. Also shown are paths of adiabatic melting (dashed arrows labelled X, Y, Z). The solid arrow shows a liquid line of descent for fractionation of olivine from one, arbitrary experimental melt composition, calculated according to the method of Weaver and Langmuir [1987]. Note that crystallization of olivine decreases MgO contents of residual liquids but does not appreciably change their FeO contents. Representative data are shown for high MgO basalts from the Kolbeinsy Ridge (K), East Pacific Rise near the Tamayo transform fault (T), and the Australian-Antarctic Discordance (A), which span most of the range in chemistry and bathymetry presented in Table 1.

Langmuir and Hanson [1980]. Experimental melt compositions of Jaques and Green [1980] are shown on the FeO/MgO diagram in Figure 5, with a melt field for pyrolite calculated by the method of Langmuir and Hanson [1980]. The new experimental data are consistent with the calculations in the sign and magnitude of the pressure dependence, as well as the inferred path of adiabatic melting. The data of Jaques and Green do not agree with the single 10-kbar point of Takahashi [1985], however, and there are some discrepancies in terms of the variations of temperature with MgO content.

Like FeO , the systematics of SiO_2 variations during melting depend on the pressure as well as the extent of melting. Experimental studies show that at any one pressure, SiO_2 increases with increasing extents of melting, to approximately 40% melting [Jaques and Green, 1980; Mysen and Kushiro, 1977]. MgO contents also increase with increased melting at any one pressure, which leads to greater extents of olivine fractionation to reach a reference value of MgO . Since olivine has a low SiO_2 content, such fractionation of olivine to lower MgO contents leads to still higher SiO_2 contents in the fractionated magma. These two

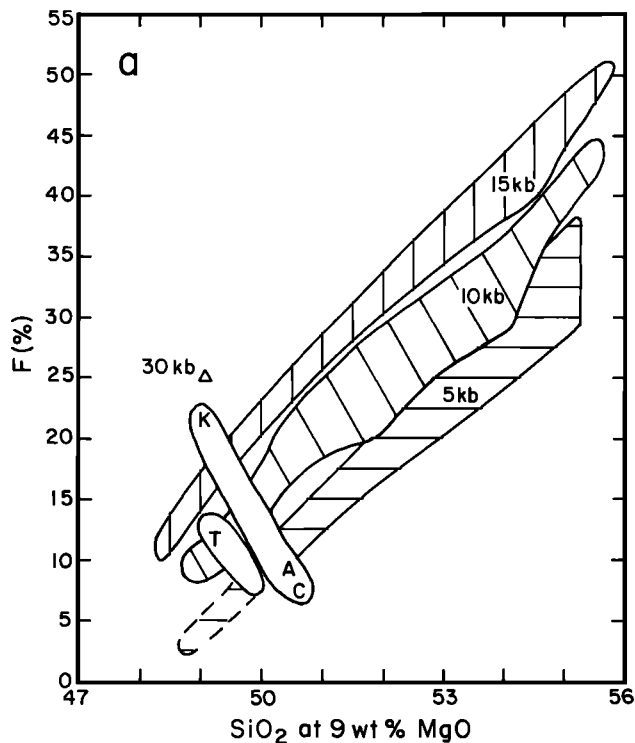


Fig. 6. (a) SiO_2 contents (wt %) calculated to 9 wt % MgO by removal of Fo90 olivine in melts from the experiments of *Jaques and Green* [1980], and *Takahashi* [1985] plotted versus the extent of melting (extents of melting for the data of *Takahashi* were constrained by Na_2O and TiO_2 abundances). The 10- and 5-kbar fields overlap slightly. Note that SiO_2 at 9 wt % MgO increases with increasing extents of melting; for the same extent of melting, melts produced at higher pressure have lower SiO_2 contents. Also shown are mean SiO_2 contents for basalts from the Kolbeinsey Ridge (K), Tamayo region of the EPR (T), the Australian-Antarctic Discordance (A), and the Mid-Cayman Rise (C). Extents of melting for these areas were estimated from their $\text{Na}_{8,0}$ contents as discussed in the text. (b) Regional averages of SiO_2 determined by plasma emission spectrometry versus $\text{Na}_{8,0}$ (from Table 1), with the exception of the SiO_2 data for Cayman and Kolbeinsey, which are from the Smithsonian microprobe (see reference 6, Table 1) and *Schilling et al.* [1983], respectively, and were corrected to a comparable basis (normalized to 100%, total FeO as Fe_2O_3 , and an interlaboratory correction factor of 0.988 applied to the Smithsonian data). Symbols as in Figure 2. Note that for the same $\text{Na}_{8,0}$ samples from the Pacific are offset to lower SiO_2 abundances, compared to samples from Atlantic and Indian ocean ridges. The bars on the one point show the standard deviation in SiO_2 for 42 analyzed samples from the Tamayo region.

additive effects produce higher SiO_2 contents in basalts evolved from parental magmas derived by greater extents of melting at a given pressure. This somewhat surprising result is illustrated in Figure 6a, and is consistent with experimental data from four laboratories [*Jaques and Green*, 1980; *Fujii and Scarfe*, 1985; *Takahashi*, 1985; *Mysen and Kushiro*, 1977]. However, the abundance of SiO_2 in the melt also depends strongly on the pressure of melting. For a given extent of melting, increased pressure causes melts to have lower SiO_2 contents (see Figure 6a).

A summary of the behavior of the major elements during melting of the mantle is presented in Table 2. When combined with planetary constraints on the mantle composition, Table 2 and associated figures allow estimates of extents and pressures of melting to be made from major

element compositions alone. The systematics can be applied to small-scale petrogenetic studies as well as to the global scale problems considered in this paper.

Application of Melting Systematics to the Global Chemistry/Depth Correlations

The global MORB data set shows the following general characteristics, as exemplified by data from shallow, "normal," and deep regions, that is, the Kolbeinsey Ridge, the East Pacific Rise near the Tamayo transform, and the Australian-Antarctic Discordance, respectively.

Regions with low $\text{Na}_{8,0}$ such as the Kolbeinsey Ridge, have relatively high FeO and $\text{CaO}/\text{Al}_2\text{O}_3$ and low SiO_2 . Conversely, regions with high $\text{Na}_{8,0}$ such as the Australian-Antarctic Discordance and the Cayman Trough, have relatively low FeO and $\text{CaO}/\text{Al}_2\text{O}_3$ and higher SiO_2 . The relative variations in $\text{Na}_{8,0}$ immediately suggest that lower $\text{Na}_{8,0}$ regions are derived by greater extents of melting. The global inverse correlation between $\text{CaO}/\text{Al}_2\text{O}_3$ and $\text{Na}_{8,0}$ is also consistent with the effects of different extents of melting, with clinopyroxene as a residual phase for most regions; however, for the area immediately around Iceland, where $\text{CaO}/\text{Al}_2\text{O}_3$ may begin to decrease slightly as $\text{Na}_{8,0}$ decreases (see Figure 2b), clinopyroxene may no longer be a residual phase. This suggests that areas erupting basalts with low $\text{Na}_{8,0}$ and high $\text{CaO}/\text{Al}_2\text{O}_3$, such as the Kolbeinsey Ridge, have undergone larger extents of melting than areas where basalts have high $\text{Na}_{8,0}$ and low $\text{CaO}/\text{Al}_2\text{O}_3$. Figure 3 shows some representative regional averages of CaO and Al_2O_3 for samples with 8.5-10 wt % MgO (to minimize the effects of fractionation) plotted against regional $\text{Na}_{8,0}$ values from Table 1; also plotted are experimentally determined melt variations in CaO and Al_2O_3

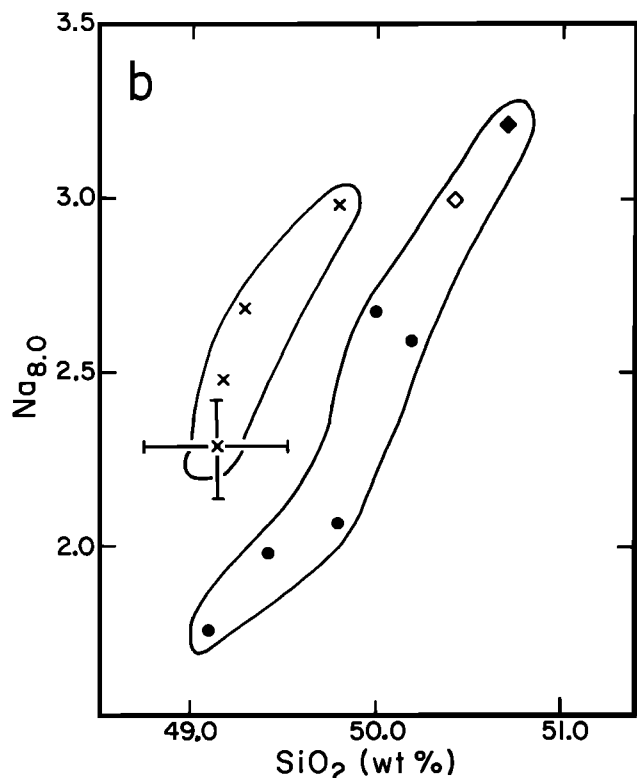


Fig. 6 (continued)

Table 2. Systematics of Melting of Spinel Lherzolite From $F=0$ to 0.30

Element	General Systematics	Instantaneous Melts in an Adiabatically Upwelling Column	Pooled Melts from an Adiabatically Upwelling Column	Figure
SiO ₂	for constant MgO, increases with F , decreases with increasing P	increases with F	decreases with increasing P_0	6a and 13
Al ₂ O ₃	decreases with F , decreases with increasing P	decreases with F	decreases with increasing P_0	3a and 4
MgO	increases with F at constant P , increases with increasing P	approximately constant	increases with increasing P_0	5
FeO	constant with F at constant P , increases with increasing P	decreases with F	increases with increasing P_0	5
Na ₂ O	decreases with F ; behaves as a moderately incompatible element	decreases with F	decreases with increasing P_0	3
CaO	increases with F while cpx is residual, then decreases with increasing F	increases with F while cpx is residual	increases with increasing P_0 while cpx is residual, then decreases	3b

versus Na₂O with progressive melting of a spinel lherzolite [Fujii and Scarfe, 1985]. Each element varies in the sense expected by different extents of melting.

Understanding the variations in FeO and SiO₂ requires consideration of the pressure of melting as well as the extent of melting. Discussion of the effects of pressure on melting systematics must, in turn, distinguish between segregation pressure and the pressure at the intersection of the solidus. In Figure 5, the lower dashed arrow (X) shows the adiabatic path of melting that would result from an upwelling diapir that intersects the mantle solidus at about 7 kbar. Magmas derived by lower extents of melting in such a diapir would have both higher Na₂O and Fe₂O relative to magmas formed by greater extents of melting in the same diapir. Thus, if FeO were controlled simply by the extent of melting in diapirs that intersected the solidus at a single pressure, one would expect to see a positive correlation between Fe₂O and Na₂O, which is not observed. A second possibility is the case where two diapirs intersect the solidus at different pressures but segregate at the same pressure. In Figure 5, diapirs X and Y intersect the solidus at >20 kbar and ≈15 kbar, respectively. If both diapirs segregated within the 10-kbar melt field, then magmas derived from the two diapirs would have approximately the same Fe₂O contents, but X, having undergone greater extents of melting would have lower Na₂O than Y would have. This scenario would therefore lead to no correlation between Na₂O and Fe₂O. Consider, last, a scenario in which a diapir that intersects the solidus at a higher pressure also segregates at a higher pressure. In Figure 5, diapirs Z, Y, and X intersect the solidus at successively higher pressures; the mean pressures of melting within each diapir will increase progressively from Z to X and lead to increasing Fe₂O, and the mean extent of melting will increase from Z to X. This scenario is consistent with the observed inverse correlation between Na₂O and Fe₂O (compare Figures 2a and 2c).

Using the Jaques and Green data to calibrate the pressure effects, the high Na₂O (low Fe₂O) data (e.g., the Australian-Antarctic Discordance) are consistent with mean

segregation pressures of about 5 kbar, while the medium Na₂O (and Fe₂O) data (e.g., EPR, Tamayo region) require mean pressures of 10 kbar. The Kolbeinsey Ridge data (low Na₂O, high Fe₂O) suggest mean segregation pressures of about 15 kbar.

Figure 5 also implies that the samples derived by higher extents of melting at higher mean pressures have undergone more fractionation of olivine prior to eruption. If the Jaques and Green [1980] data are pertinent, MgO contents of primary magmas range from about 10 wt % (≈14 cation mole %) for the deep ocean regions produced by the smallest extents of melting, and up to 15 wt % (≈20 cation mole %) for the shallowest regions around Iceland, produced by larger extents of melting.

The SiO₂ variations with pressure and extent of melting are subtle, and to discern their systematics in the data requires good analytical precision. Lamont plasma data on glasses are precise for SiO₂ to ± 0.2 wt %, substantially better than microprobe data. Figure 6 shows regional averages of SiO₂ for samples with 8.5–10 wt % MgO versus Na₂O (from Table 1) for all of the areas for which there are plasma data, with the addition of data from the literature for the critical areas at the extreme chemical and depth ranges (Mid-Cayman Rise and Kolbeinsey Ridge), for which we have used the Smithsonian microprobe data [Thompson *et al.*, 1980] and the whole rock data of Schilling *et al.* [1983].

There is a positive correlation between Na₂O and SiO₂ (Figure 6b), and apparently the data from the Pacific are slightly offset to lower SiO₂. If the global chemical variations were produced by different extents of melting at a constant equilibration pressure (i.e., constant pressure of melt segregation), one would expect an inverse correlation between SiO₂ and Na₂O, contrary to what is observed. Thus the SiO₂ data, like the FeO data, suggest that the areas where lower extents of melting occurred also melted at lower mean pressures. The SiO₂ data can be used to quantitatively constrain mean pressures of melting and suggest a pressure range of 5–20 kbar (compare Figures 5a and 5b), which is approximately the same as that inferred from FeO.

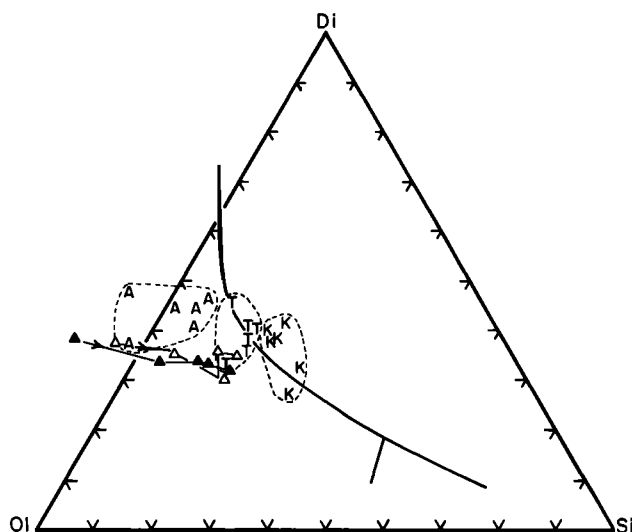


Fig. 7. Pseudo-ternary diagram of normative diopside-olivine-silica (Di, Ol, Si) projected from plagioclase; calculated according to the method of Walker *et al.* [1979]. K, T, and A are as in Figure 4. Also shown are the results of progressive melting of two synthetic spinel lherzolites at 10 kbar (open and solid triangles) reported by Fujii and Scarfe [1985]. Arrows indicate direction of compositional change in the melts with increasing extents of melting.

The Al_2O_3 abundances in MORB also support these estimates of the range in pressures of melting. In addition to the inverse variation between Al_2O_3 and extent of melting (Figure 3), Al_2O_3 abundances show a subtle inverse correlation with pressure (Figure 4). The high Al_2O_3 contents of the MORB data suggest that the mean pressure of melting ranges from >5 to <15 kbar, if the Jaques and Green data are pertinent (Figure 4). Thus all the major element data are remarkably consistent with an origin by different extents of melting over different pressure intervals; melts produced by greater extents of melting appear to be generated at higher pressures of melting.

Implications for Use of the Walker/Stolper Projected Phase Diagram

In the discussion above, major element systematics during melting, as a function of both pressure and extent of melting, have been examined element by element. In order to investigate how the major elements vary in concert, a common approach has involved the use of the pseudo-ternary of Walker *et al.* [1979] and Stolper [1980]. Figure 7 shows the plagioclase projection of the pseudo-ternary with the data of Fujii and Scarfe [1985] for compositions produced by equilibration of basalt with spinel lherzolite over a range of temperatures at 10 kbar. Melt compositions at the lowest temperatures, analogous to smaller extents of melting, plot on the silica-undersaturated side of the pseudo-ternary. With progressively larger extents of melting at a single pressure, the compositions become more enriched in the silica component. This finding was also noted by Takahashi and Kushiro [1983] and Presnall and Hoover [1984].

The data clearly show that there are no five-phase invariant points on this projected phase diagram (see, e.g., Fujii and Scarfe [1985]). The positions of the so-called isobaric invariant points were inferred from the disappearance of clinopyroxene as a liquidus phase in experimental charges [Stolper, 1980]. Since the points are not invariant, they simply show the point along melting

curves where clinopyroxene melts out of the residue. With increased pressure the melting curves shift toward the olivine apex [Stolper, 1980; Takahashi and Kushiro, 1983; Presnall and Hoover, 1984].

Also shown in Figure 7 are basalts from three regions encompassing the range in chemistry and bathymetry presented in Table 1. The relative positions of the three type regions on this diagram are consistent with the experimental data suggesting varying extents of melting. The Kolbeinsey data, which the chemical systematics suggest are derived by greater extents of melting at higher mean pressures, are highest in the silica component, (although lowest in SiO_2).

Thus the position of a parental magma on this diagram is determined by two competing effects: increasing extents of melting move parental magma compositions toward silica, while increased pressures of melting shift melts away from silica and toward the olivine apex. The data suggest that the dominant control on position of olivine \pm plagioclase-saturated magmas on this diagram relative to silica is the extent of melting rather than the pressure of melting. Thus the use of this diagram to constrain pressures of melting is not straightforward. For constraints on pressure, it appears to be simplest to examine variations in the abundance of individual oxides that are pressure-sensitive, such as FeO and SiO_2 .

Quantitative Constraints on the Extents of Melting

The major element data allow upper limits to be placed on the extents of melting for the different oceanic regions. Data from primitive mantle nodules [Jagoutz *et al.*, 1979], peridotite suites [Frey *et al.*, 1985], and chondritic considerations [Hart and Zindler, 1987] suggest that Na_2O in the undepleted mantle is 0.30 ± 0.03 , CaO about 3.2 wt %, and Al_2O_3 about 4.1 wt %. Since the range in Na_2O for the basalts after correction for olivine fractionation is 1.5 wt % Na_2O (for the Kolbeinsey Ridge) to 3.4 wt % Na_2O (for the Cayman Trough), this would imply a range in extent of melting (F) from 0.20 to 0.09, if sodium were perfectly incompatible. Because Na_2O is not perfectly incompatible, however, these values represent upper limits on F for their respective regions. Upper limits can also be obtained for CaO and Al_2O_3 . How close these limits approach actual values depends on how compatible the element is during melting. For the Kolbeinsey Ridge, the upper limits on F are 0.32 for Al and 0.29 for Ca. For the Mid-Cayman Rise the upper limits are 0.25 for Al and 0.33 for Ca. Thus, for the lowest extents of melting beneath Cayman, Ca and Al clearly behave more compatibly and do not give useful upper limits, while for greater extents of melting beneath Kolbeinsey Ridge the upper limits are much closer to that provided by Na.

If the MORB source is more depleted than primitive mantle, these upper limits would be decreased in proportion to the depletion of the source. Thus the bounds of $<9\%$ to $<20\%$ melting are difficult to exceed. The upper limit of 20% melting is probably a good estimate of the extent of melting required to produce the Kolbeinsey data, since Na is likely to be very incompatible once clinopyroxene disappears from the residue. For the lower extents of melting, if one assumes $<15\%$ clinopyroxene in the residue and a distribution coefficient for Na_2O in clinopyroxene of 0.15, then one obtains an estimate of 7–8% melting for the highest Na_2O melts. Thus, the likely range of F to account

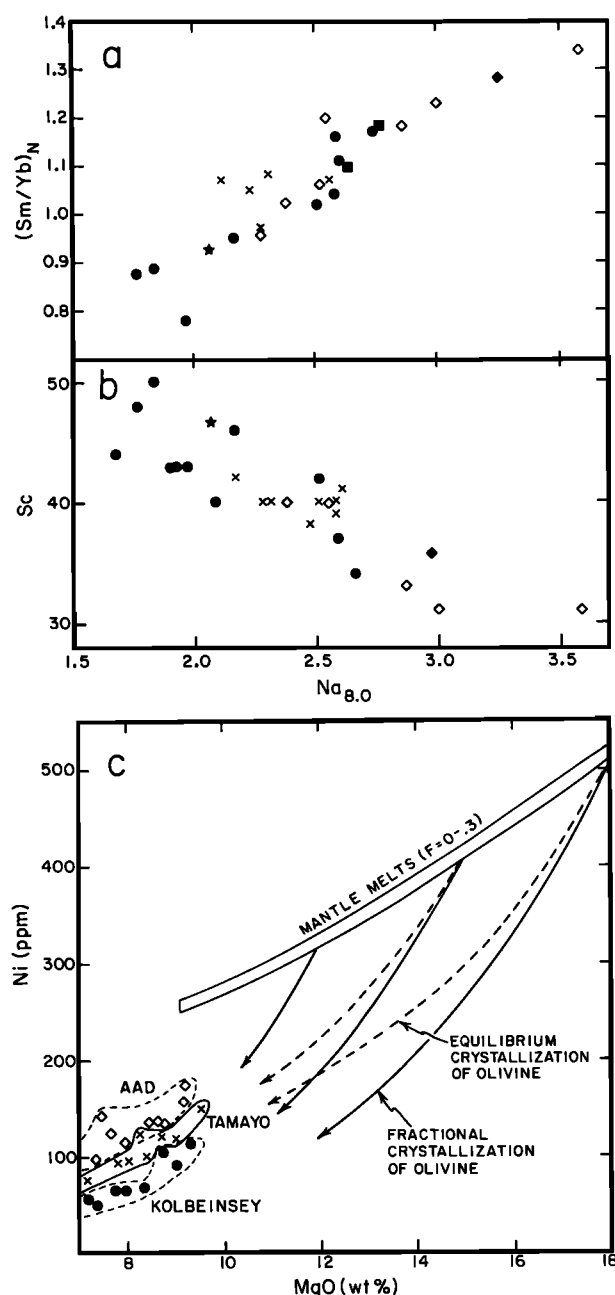


Fig. 8. $\text{Na}_{8.0}$ versus (a) $(\text{Sm}/\text{Yb})_N$ and (b) Sc (ppm). Symbols are as in Figure 2. $(\text{Sm}/\text{Yb})_N$ was calculated only for samples with $(\text{La}/\text{Ce})_N \leq 1$. Sc abundances are for samples with >7.5 wt % MgO. Stars are for samples from 140 Ma crust, as discussed in the text. Data are from Schilling *et al.* [1983], E. Klein *et al.* (manuscript in preparation, 1987), Rice *et al.* [1980], Bryan *et al.* [1981], Humphris *et al.* [1985], Price *et al.* [1986], Schilling *et al.* [1982], Fryer *et al.* [1981], Perfit *et al.* [1987], leRoex *et al.* [1983], Bender *et al.* [1984], Kay *et al.* [1970], Schilling [1969], Dickey *et al.* [1977], Saunders and Tarney [1979], and M. Perfit and G. Waggoner (unpublished data, 1986). (c) Ni (ppm) versus MgO (wt %) for samples from Kolbeinsey Ridge (solid circles), EPR south of the Tamayo transform (crosses), and the Australian-Antarctic Discordance (open diamonds). Data from Schilling *et al.* [1983], Bender *et al.* [1984], C.H. Langmuir and J.F. Bender (unpublished data, 1987), and E. Klein *et al.* (manuscript in preparation, 1987). Also shown is a field for melting 0-30% of the mantle, after Hart and Davis [1978] and Nabelek and Langmuir [1986]. Arrows indicate changes in residual liquid compositions for equilibrium (dashed) and fractional (solid) crystallization of olivine from various primary magma compositions. Note that the three MORB suites, AAD, Tamayo, and Kolbeinsey, must be derived from parental magmas with progressively higher MgO and Ni contents, in agreement with Figure 5.

for the global range in data is approximately 8-20% melting.

Trace Element Consistency With the Partial Melting Hypothesis

Global systematics of trace element variations for elements that are not highly incompatible support the inferences from major elements presented above. Figure 8a shows regional averages of available data for Sc abundances and $(\text{Sm}/\text{Yb})_N$ ratios versus $\text{Na}_{8.0}$. In order to minimize the effects of source heterogeneity or source volume differences for strongly incompatible elements [e.g., McKenzie, 1985; O'Hara, 1985; Zindler and Jagoutz, 1987], $(\text{Sm}/\text{Yb})_N$ ratios are plotted only for regions that exhibit $(\text{La}/\text{Ce})_N < 1$. Because Sm, Yb, and Sc are only moderately incompatible during melting of mantle assemblages, these element can be modeled in a simpler way than highly incompatible elements because their abundances in the source should approximate those of the bulk mantle and are unlikely to be substantially modified by processes such as mantle metasomatism, removal of small amounts of melt, or formation of the continents. The equation for batch melting of the mantle where the bulk distribution coefficient for the mineralogy of the solid that is melting differs from that of the bulk mantle is

$$C_L / C_0 = 1 / [D_0 + F(1 - \phi)] \quad (1)$$

where C_L is the abundance of the element in the magma, C_0 is its abundance in the source, F is the fraction of melt, D_0 is the bulk distribution coefficient at the onset of melting, and ϕ is the distribution coefficient of the actual portion of the solid that is being converted into liquid [Shaw, 1970]. Assuming that ϕ is constant, then for any two extents of melting, F_1 and F_2 , manipulation of equation (1) leads to:

$$D_0 = C_0 * (F_2 C_{L2} - F_1 C_{L1}) / [C_{L2} * C_{L1} (F_2 - F_1)] \quad (2)$$

Using the two extreme values of F estimated above from the major elements, C_0 's estimated from primitive mantle abundances, and the two C_L 's from the measured basalt abundances, D_0 can be determined from equation (2), and ϕ from equation (1). Using C_0 abundances of 17, 0.38, and 0.42 ppm for Sc, Sm, and Yb, respectively [Jagoutz *et al.*, 1979], and values of F of 0.08 and 0.20 for the two end-members in the MORB array, we obtain values for D_0 of 0.69, 0.035, and 0.097 for these three elements, and values for ϕ of 2.75, 0.18, and 0.32. These values for both D_0 and ϕ are appropriate provided clinopyroxene is the dominant Sc-, Sm-, and Yb-bearing mineral entering the melt. Depending upon the mineral/melt distribution coefficients used [e.g., Irving, 1978; Henderson, 1982], the values for ϕ suggest that approximately 70% of the melt is composed of clinopyroxene, and 30% is composed of olivine and orthopyroxene. Furthermore, because the calculated D_0 's are threefold to fivefold smaller than the values for ϕ , these calculations suggest that the original bulk source contained ~15% clinopyroxene, which is consistent with primitive upper mantle estimates [Jagoutz *et al.*, 1979].

Hart and Davis [1978] presented data which showed that various basalt suites had different MgO-Ni characteristics, and Nabelek and Langmuir [1986] emphasized the substantial differences in Ni abundances among MORB suites. Both papers suggested the MgO-Ni systematics might be related to melting of the mantle under varying

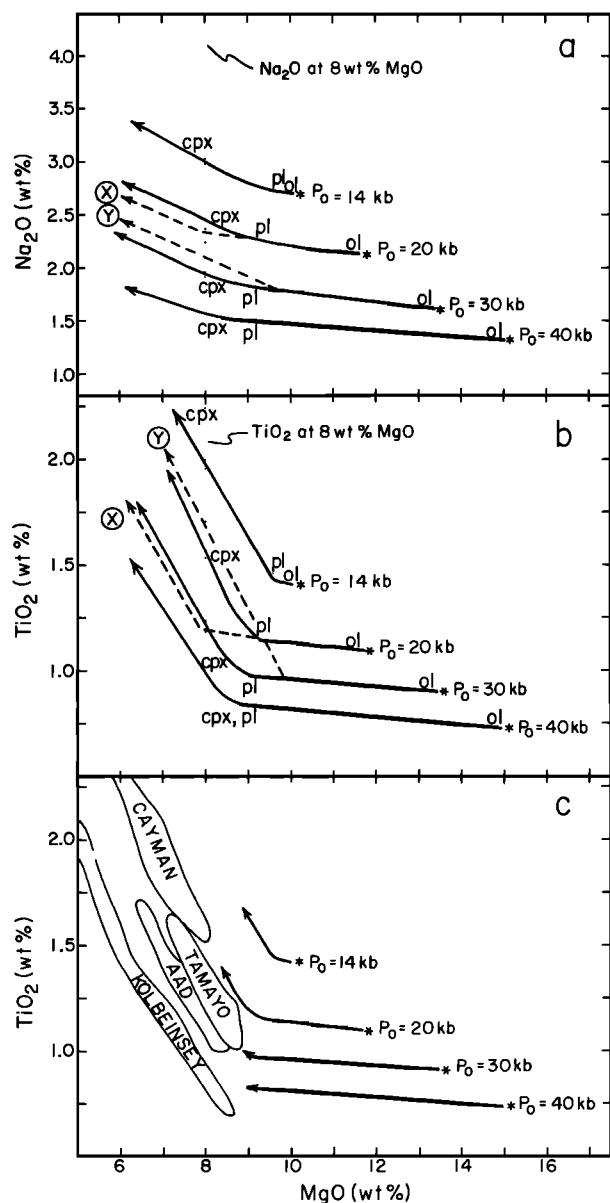


Fig. 9. MgO versus (a) Na₂O, and (b) and (c) TiO₂. In Figures 9a and 9b, asterisks indicate parental magma compositions calculated for $P_0 = 40, 30, 20$, and 14 kbar, as discussed in the text; solid curves are liquid lines of descent calculated for each parental magma composition, according to the method of Weaver and Langmuir [1987]; locations of ol, pl, and cpx along each liquid line of descent indicate calculated appearances of olivine, plagioclase, and clinopyroxene; dashed curves, labeled X and Y, graphically show the effects of an approximate 1 wt % decrease or increase in the MgO contents where plagioclase joins olivine on the 20- and 30-kbar liquid lines of descent; the dotted line at 8 wt % MgO is shown for reference and indicates the approximate location of a calculated value of Na₂O or TiO₂ for each liquid line of descent. Note that for Na₂O (Figure 9a), a change of ± 1 wt % MgO where plagioclase joins olivine on the liquidus (X and Y) has little effect on the apparent, relative Na₂O abundances in the 20- and 30-kbar parental magmas; in contrast, due to the abrupt bends in the liquid lines of descent for TiO₂ (Figure 9b), a change of ± 1 wt % MgO where plagioclase joins olivine on the liquidus reverses the apparent, relative TiO₂ contents in their respective parental magmas. In Figure 9c are shown fields for data on basalts from the Mid-Cayman Rise, EPR south of the Tamayo transform, Australian-Antarctic Discordance, and Kolbeinsey Ridge; arrows indicate portions of the liquid lines of descent shown in Figure 9b.

conditions. Figure 8c shows data for MgO versus Ni for three normal MORB suites representing the range in axial depth shown in Table 1. Also shown is the range of mantle melt compositions, calculated as by Nabelek and Langmuir [1986], and three trajectories showing fractionation of olivine from different parental magmas. For a given MgO content the suite with the lowest Ni content is derived from parental magmas with the highest MgO contents. Higher MgO would be associated with parental magmas generated by greater extents of melting at higher pressure. The order of the trends in Figure 8c is thus consistent with the major element constraints presented above.

We turn last to the systematics of TiO₂. Because TiO₂, like Na₂O, behaves as a moderately incompatible element during melting, one would expect a correspondence between the abundances of these two oxides from region to region. This is partially true: high TiO₂ and Na₂O abundances occur in basalts from the Mid-Cayman Rise, and low TiO₂ and Na₂O abundances occur in samples from the Kolbeinsey Ridge (Figure 9c). However, in order to compare fully TiO₂ abundances in suites of variably fractionated basalts from different regions, we must correct TiO₂ contents for shallow-level fractionation to a comparable value, as we did for Na₂O.

The inaccuracies in correction for low pressure fractionation depend on the trajectory of the liquid line of descent as fractionation proceeds. On a plot of MgO versus Na₂O, olivine fractionation produces a smooth, gradual increase in Na₂O, with decreasing MgO. When plagioclase and then clinopyroxene join olivine on the liquidus, the slope of this liquid line of descent increases only slightly because clinopyroxene and particularly plagioclase remove Na₂O from the liquid (Figure 9a). Because the slope of the liquid line of descent does not change appreciably as new phases appear, it is possible to correct the Na₂O abundances in variably fractionated basalts to a comparable value of MgO with minimal error (Figure 9a).

The liquid line of descent for TiO₂, however, differs markedly from that of Na₂O. During olivine fractionation, on a plot of MgO versus TiO₂, TiO₂ increases slightly with decreasing MgO; when plagioclase joins olivine on the liquidus, however, the slope of the liquid line of descent changes abruptly, and TiO₂ increases substantially with decreasing MgO (Figure 9b). Thus, in contrast to Na₂O, the value of TiO₂ depends critically on the precise MgO content where plagioclase joins olivine on the liquidus (see Figure 9b). The location of this abrupt bend in the liquid line of descent, however, depends on pressure and water content as well as composition. For example, a higher water content suppresses the appearance of plagioclase to lower values of MgO. Indeed, J.M. Sinton and P. Fryer (Mariana trough lavas from 18°N and the origin of back arc basin basalts, submitted to *Journal of Geophysical Research*, 1987) and Fryer et al. [1981] have argued that the low abundances of TiO₂ in Marianas back arc basin lavas result from the suppression of plagioclase crystallization to lower MgO contents.

This sensitivity of TiO₂ abundances to the precise MgO where plagioclase appears on the liquidus may in part explain the imperfect relationship between TiO₂ content and the extent of melting determined by other major elements. Samples from the Kolbeinsey Ridge, Tamayo region, and the

Mid-Cayman Rise show the expected relative TiO_2 abundances, but samples from the Australian-Antarctic Discordance appear to be anomalously low in TiO_2 . This problem also exists for FeO and may in part explain the greater scatter of the Fe_2O_3 diagram (Figure 2c).

The TiO_2 discrepancy may also arise in part from the discrepant behavior of the "incompatible elements" as a group. These elements (including, e.g., K and Ba) are very sensitive to extraction or addition of small melt fractions, and do not show clear global correlations with depth. Some very shallow regions, such as the Kolbeinsey Ridge, are highly depleted in incompatible elements [Schilling *et al.*, 1983], while shallow hot spots are often enriched. In addition, axial hot spots, such as Iceland, are also often high in TiO_2 and have $\text{TiO}_2/\text{Na}_2\text{O}$ ratios in excess of fertile mantle sources. Since the partition coefficient for Na_2O appears to be less than that of TiO_2 during mantle melting, this high ratio is often difficult to reconcile with melting systematics, and the TiO_2 data are not completely consistent with the inferences from the major elements.

Summary

In summary, major element and much trace element data are consistent with the derivation of the broad global variations in MORB chemistry by melting between 8 and 20% of the mantle with clinopyroxene present as a residual phase for all but the very greatest extents of melting. Melts derived by lower extents of melting equilibrate at lower pressures in the mantle. The inferred extents of melting correlate with the depth of the spreading center axes. Some hot spot centers are consistent with these conclusions, but others exhibit anomalous behavior in some elements. It is conceivable that these latter anomalies are caused by modifications of the phase equilibria by volatiles [Schilling *et al.*, 1983], but they may also reflect major element heterogeneity in the mantle source. Incompatible element abundances are strongly affected by processes independent of those causing the global major element variations.

DISCUSSION

Constraints on Mantle Temperature and Melting Processes

It has long been suggested that melting beneath ocean ridges occurs in response to adiabatic upwelling of the mantle beneath the ridge. The extents of melting resulting from adiabatic decompression of mantle material have been calculated frequently, using constraints from experimental data, thermodynamic properties of solid and liquid, and mantle temperature estimates [e.g., Verhoogen, 1954; Cawthorn, 1975; Ahern and Turcotte, 1979; McKenzie, 1984]. The bottom line in these calculations is the percentage of melt produced per kilobar of pressure release after intersection of the mantle solidus. The percentage of melt will vary slightly as a function of pressure, but in view of the uncertainties in heat capacities, heats of fusion, and the extent of melting per degree above the solidus, a constant value may be warranted. Ahern and Turcotte [1979] calculate this percentage to be 1.2% melting per kilobar of pressure release, and we use their value. The calculations of McKenzie [1984] range from 0.72 to 1.5% melt/kbar, with a best estimate of ~0.95% melt/kbar. These authors and, in addition, Reid and Jackson [1981] and Sleep and Windley [1982] made the additional point that the thickness of the

ocean crust should relate to the amount of melt produced during upwelling beneath the ridge, although this depends on the mantle flow regime. Since we have independent estimates from the basalt chemistry of extents and pressures of melting, it is of interest to compare the thermal constraints from the major and trace element chemistry with the adiabatic upwelling model and to determine what sort of melting model is consistent with the petrological data.

In theory, there are several possible mechanisms by which varying extents of melting could occur beneath ridge axes and thus generate the observed spectrum of major element variations. Three possible mechanisms are illustrated in Figure 10. First, all melts might be generated along a single mantle thermal gradient but segregate at different depths and pressures (Figure 10a). This model is inconsistent with the data because it requires that the largest extents of melting segregate the shallowest, while the data suggest the opposite. In the second model, a single mantle temperature gradient acts upon different mantle compositions (Figure 10b). In this case, the more depleted mantle, with lower Na_2O , would intersect its solidus shallower and would melt less, leading to higher Na_2O . The effects of melting and source composition would therefore have opposite effects on Na_2O , and the net result is not obvious. In the third model, different regions of the mantle are at different temperatures at the same depth and therefore intersect the mantle solidus at different depths upon upwelling (Figure 10c). This is the model considered by Cawthorn [1975], Ahern and Turcotte [1979], Langmuir and Hanson [1980], Sleep and Windley [1982], and McKenzie [1984] and is the one we consider in more detail in light of our major element chemical constraints.

In the simplest version of this model, a diapir rises and undergoes partial melting and the melt segregates at some constant pressure beneath the ridge. This model is implicit in many discussions of mantle melting where the "segregation pressure" of MORBs is discussed [e.g., Presnall *et al.* 1979; Elthon and Scarfe, 1984]. If this were the case, however, one would expect all the major element data to be related by different extents of melting at a single pressure, the final pressure of equilibration. The major element data, however, are not consistent with a constant pressure of melt segregation. On the contrary, segregation pressures appear to vary, and there is a fundamental relationship between pressure and extent of melting. Those magmas derived by greater extents of melting record deeper segregation from their mantle sources.

Integrated Melting Column

A way to reconcile the data with the simple adiabatic melting model is to envision a process in which the melt is sampled from throughout the ascending mantle column and the erupted magma represents a mean of the melts from the entire column. For this model to be physically realistic, it requires that melts can ascend rapidly relative to the mantle matrix. The model is essentially how Ahern and Turcotte [1979] and McKenzie [1984] envisioned melting to occur beneath ocean ridges. In regions where the mantle intersects the solidus deeper, the melting column extends to greater depths, so the magmas will be generated over a higher mean range of pressures. In such a model, the mean extent of melting is substantially less than the maximum

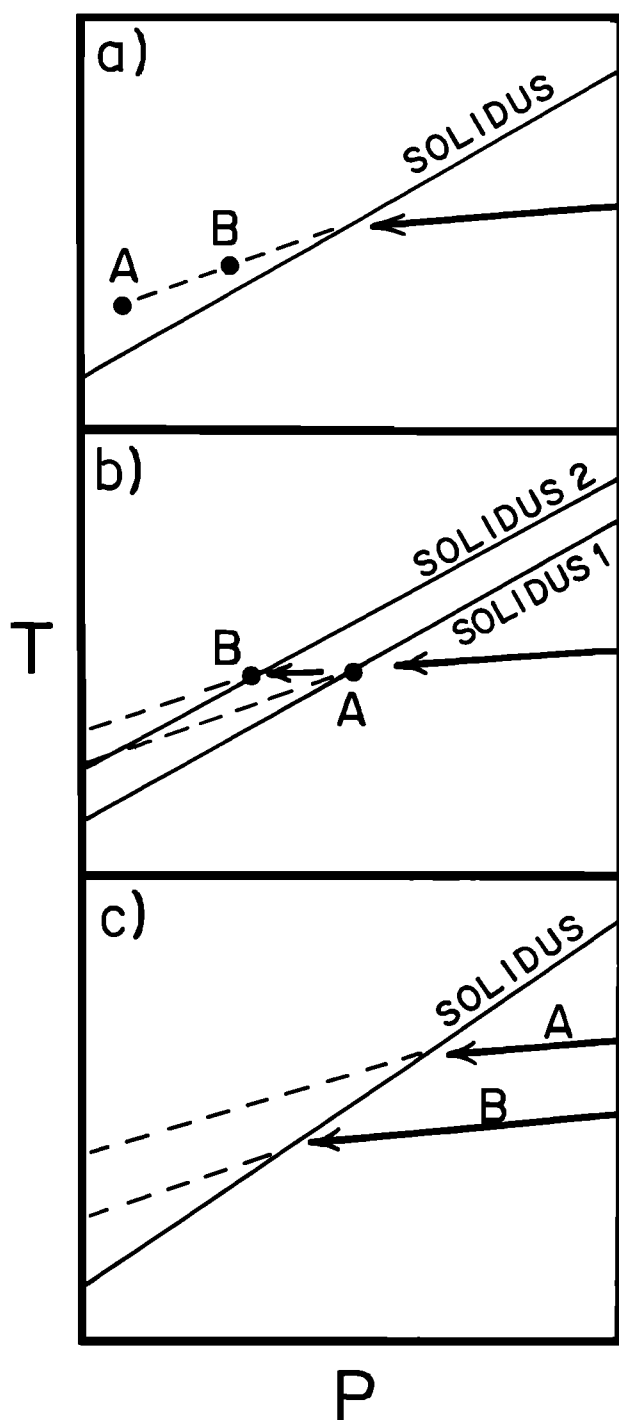


Fig. 10. Schematic mantle pressure versus temperature profiles. In Figures 10a-10c, "A" and "B" represent the paths followed to generate magmas erupted along shallow or deep ridges, respectively. (a) The mantle is characterized by a single thermal gradient, the solidus is intersected at the same pressure everywhere, but magmas segregate at different depths and therefore exhibit different extents of melting. (b) The mantle is characterized by a single thermal gradient but there are markedly different mantle compositions beneath different ridges; "A" intersects the solidus deeper, due to its more fertile nature, and melts more; "B" represents more depleted mantle that intersects its solidus shallower and melts less. (c) Different regions of the mantle are at different temperatures at the same depth and therefore intersect the solidus at different pressures, depths, and temperatures. "A" represents a hotter region of mantle which therefore intersects the solidus deeper and melts more; "B" represents a cooler mantle region which intersects the solidus shallower and melts less. As discussed in the text, Figure 10c depicts our preferred model.

extent of melting reached at the top of the column. Thus clinopyroxene could be absent from the residual mantle immediately beneath the ridge, although the erupted magma (the integrated melt from the entire column) may still retain the chemical signature of residual clinopyroxene (or garnet) from deeper in the melting column.

Qualitatively, this model is clearly consistent with the data, but it would be useful to obtain quantitative constraints. In realistic terms, a quantitative model is difficult because it entails melt and solid ascending at different rates, with the two interacting as further melting proceeds. In addition, the rates of ascent of melt and solid may change as a function of melt fraction, and some component of lateral flow of melt beneath the ridge may occur. It is useful, however, to see how well a conceptually simple model accounts for the data.

This simplified model can be envisioned in the following way. An ascending mantle diapir begins melting upon intersection of the solidus and continues to melt with decreasing pressure until a final pressure of melting is reached. Thus prior to melt segregation the melting column extends from the solidus to the final pressure of melting. Within this column, the amount of melt present at a particular depth (the instantaneous melt) is governed by the difference in pressure relative to the solidus. The chemistry of each instantaneous melt is governed by the extent of melting by which it was produced and the pressure of its location in the column. If instantaneous melts segregate from throughout the column and pool at shallow depth, the pooled melt will represent a weighted mean of the compositions of all instantaneous melts. It may be necessary to emphasize that the chemical data require substantial mean pressures of mantle equilibration, far below the crust, which implies that melts can ascend without further chemical interaction with the mantle matrix. This has implications for the mechanisms of ascent, but may also result because the overlying mantle is always more depleted and cooler than the immediate source of the melt.

Quantitative Evaluation of the Integrated Melting Column

Several authors in the last 15 years have calculated the extent of melting resulting from adiabatic ascent in the mantle [e.g., Cawthorn, 1975; Ahern and Turcotte, 1979; Sleep and Windley, 1982; McKenzie, 1984]. In order to relate these calculations to petrology, it is useful to define mean pressures and extents of melting that occur within a melting column.

If the pressure of intersection of the solidus is P_0 , and the final pressure of melting is P_f , then there exists a function $F(P)$ that gives the amount of melt present at any pressure between P_0 and P_f . The total amount of melt (F_T) present within a unit column is then

$$F_T = \int_{P_0}^{P_f} F(P) dP \quad (3)$$

The mean fraction of melting, \bar{F} , is the total amount of melt in the column divided by the column height:

$$\bar{F} = \left[\int_{P_0}^{P_f} F(P) dP \right] / (P_0 - P_f) \quad (4)$$

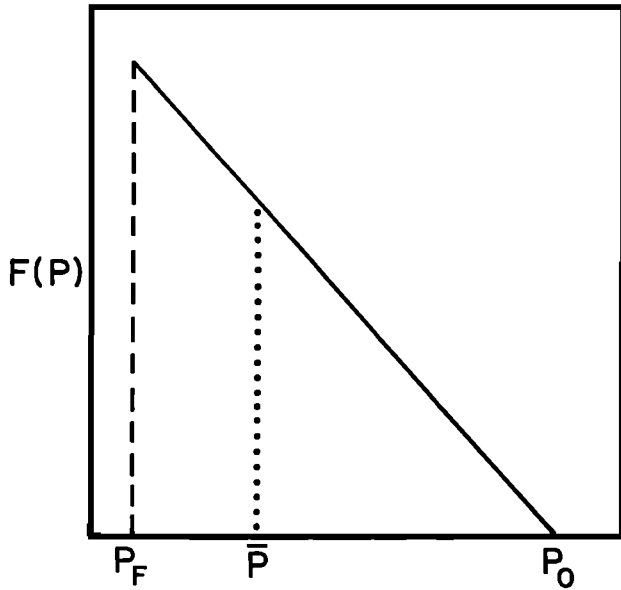


Fig. 11. Schematic representation showing $F(P)$, the amount of melt present at a particular pressure P for ascending mantle which intersects the solidus at pressure P_O and melts no further at pressures less than P_f . In calculations presented in the text, $F(P)$ is assumed to be 1.2% melt/kbar pressure release. The total amount of melt present above the solidus, F_T , as discussed in the text, is equal to the area under the diagonal line. Also shown is the mean pressure of melting, \bar{P} , defined as the pressure at which half of the melting occurs shallower and half deeper than \bar{P} .

$F(P)$ is a complex function but can be approximated by a constant value of 1.2% melt produced per kilobar of pressure release at every depth within the ascending column [Ahern and Turcotte, 1979]. Using this approximation, the amount of melt present at any pressure P , $F(P)$, is $[0.012 \cdot (P_O - P)]$. Then:

$$F_T = \int_{P_O}^{P_f} F(P) dP = \int_{P_O}^{P_f} (0.012P_O - 0.012P) dP$$

$$= 0.006 \cdot (P_O - P_f)^2 \quad (5)$$

and the mean fraction of melting is:

$$\bar{F} = 0.006 \cdot (P_O - P_f) \quad (6)$$

Note that in equations (5) and (6) the constant has units of kbar^{-1} . Thus, in (5) the total amount of melt has units of kbar , which can be converted to crustal thickness once the mean column density is known (see appendix).

One can define the mean pressure of melting, \bar{P} , as that pressure where half of the melt is produced shallower and half deeper than \bar{P} (Figure 11). Then it can be shown that

$$\bar{P} = P_O - 0.707 \cdot (P_O - P_f) \quad (7)$$

If mantle ascends all the way to the base of the crust, then the final pressure of melting corresponds to the pressure at the base of the crust. Because we assume that the total amount of melt produced, F_T , segregates to form the crust, then equation (5) gives crustal thickness D_C (in units of kbar). (Note that Ahern and Turcotte [1979] and McKenzie [1984] used $P_f = 0$ and thus substantially overestimate crustal thickness, particularly for higher values of P_O .) If

the contribution of water pressure is ignored, then P_f can be determined simply by setting it equal to crustal thickness. Thus

$$P_f = 0.006 \cdot (P_O - P_f)^2 \quad (8)$$

Thus equations (5)-(8) give the crustal thickness, the mean extent of melting, the mean pressure of melting, and the final pressure of melting in terms of the initial pressure of intersection of the solidus.

Figure 12 plots the results of these calculations. For an ascending mantle column the mean amount of melting, the mean pressure, and the crustal thickness are plotted as a function of pressure of intersection of the solidus (P_O). For mean melting of 8%, the pressure of intersection of the solidus is 14 kbar, the mean pressure is 4.8 kbar and the crustal thickness 3.6 km. For mean melting of 20%, the pressure of intersection of the solidus is 40 kbar, the mean pressure is 16.5 kbar and the crustal thickness is 22.5 km. In contrast to the simple adiabatic model that assumed a constant pressure of melt segregation, these mean pressures are similar to those inferred from the FeO and SiO_2 systematics presented above. Thus independent approaches

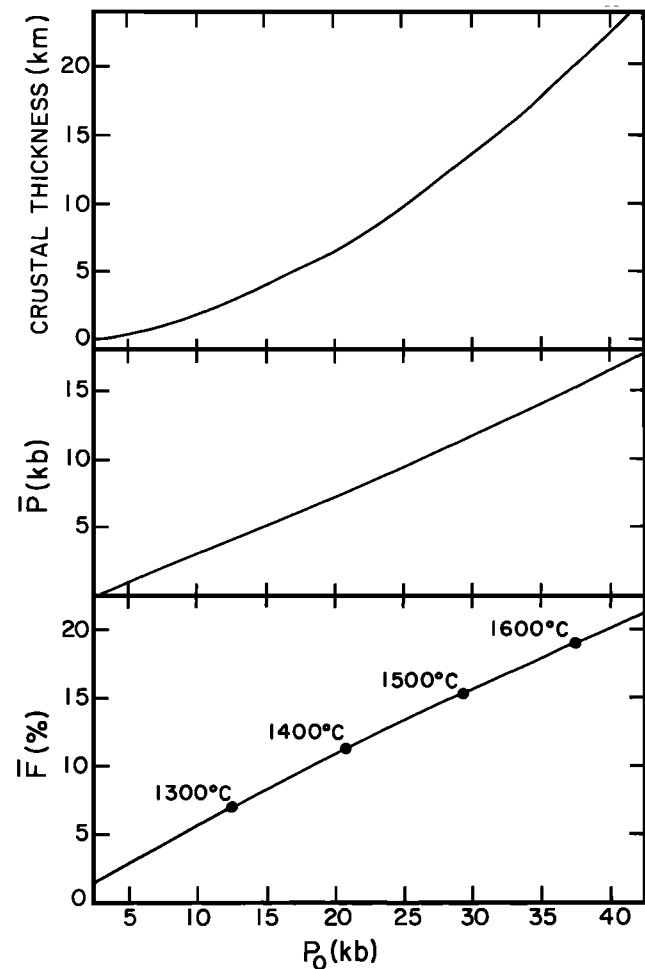


Fig. 12. Results of calculations discussed in the text, showing P_O , the initial pressure of intersection of the solidus, versus \bar{F} (the mean percentage of melt produced in the ascending diapir), \bar{P} (the mean pressure of melting), and the total crustal thickness produced, assuming complete segregation. Also shown are mantle temperatures at the intersection of the solidus, assuming a mantle solidus slope of 12°C/kbar .

of simple thermal modeling of the melting process and evaluation of MORB chemistry lead to consistent results.

The model presented above has specific implications for mantle temperatures. Assuming a solidus temperature of 1150°C at 1 atm and a solidus slope of 12°C/kbar [e.g., *Takahashi and Kushiro*, 1983], then between areas undergoing minimum and maximum extents of melting, thermal differences of ~300°C at their solidi (Figure 12) and ~250°C at equivalent depths below the solidus (see Figure 10c) are implied, provided the ascending mantle is thermally isolated from its surroundings.

BASALT CHEMISTRY, CRUSTAL THICKNESS, AND AXIAL DEPTH

The calculations presented in Figure 12 combined with the systematics of major element variations during partial melting can be used to calculate the relationships among basalt chemistry, crustal thickness, and axial depth. Calculation of basalt chemistry requires integrating melt compositions over the entire melting column. These compositions can then be used to calculate crustal density, from which crustal thickness can be calculated from equation (5). Calculation of axial depth requires knowledge of the thickness and density of the mantle residue as well as the crust, and in addition must take into account the contribution from mantle temperature, since ridges underlain by hotter mantle would be shallower simply due to thermal effects alone. These calculations are dealt with in turn in the following sections.

Calculation of Integrated Melt Compositions

In order to estimate the composition of the integrated (pooled) melts, it is necessary to determine the abundance of each element in all instantaneous melts throughout the (polybaric) melting column. Results of mantle melting experiments cannot be applied directly to this problem, however, because the experiments report changes in melt composition with increasing extents of melting at a fixed pressure. The results of these isobaric melting experiments, however, can be used to estimate polybaric melting systematics by using the value of 1.2% melt/kbar to determine the amount of melt present at a particular pressure; the isobaric melting experiments can then be used to determine the compositions of the instantaneous melt at that particular pressure and extent of melting. For this, results on the progressive isobaric melting of peridotitic compositions have been plotted as the abundance of each of the oxides SiO₂, Al₂O₃, FeO, and CaO versus extent of melting for each pressure. A similar approach to calculating mantle melting has been taken by D. McKenzie (personal communication, 1986). We have used data from various experimental studies [e.g., *Takahashi*, 1985; *Mysen and Kushiro*, 1977] where changes in melt composition versus extent of melting have been (or can be) determined, but we have placed particular emphasis on the pyrolite melting studies of *Jaques and Green* [1980]. Absolute concentration values for CaO, Al₂O₃, and FeO have been adjusted to more recent estimates of bulk silicate mantle composition [e.g., *Hart and Zindler*, 1987; *Jagoutz et al.*, 1979], and the melt compositions changed proportionately. MgO was calculated following the method of *Langmuir and Hanson* [1980] using the calculated FeO contents. For illustrative purposes, isobaric melting data for SiO₂ are shown in Figure 13a and

estimated polybaric melting curves ($C_i(F)$) for intersection of the solidus at 40, 30, 20, and 14 kbar are shown in Figure 13b.

The experimental data on the less abundant oxides Na₂O and TiO₂ are less reliable and the pyrolite abundances differ from mantle abundances by a factor of two. For these two elements, therefore, the polybaric melting paths for Na₂O and TiO₂ are given by equation (1); D_o 's and ϕ 's have been estimated from the experimental data of *Takahashi and Kushiro* [1983]. The K_d 's for Na₂O in clinopyroxene and orthopyroxene have been taken as 0.15 and 0.04; and K_d 's for TiO₂ in clinopyroxene and orthopyroxene were taken as 0.15 and 0.1. D_o 's and ϕ 's have been calculated assuming that Na₂O and TiO₂ are partitioned only into clinopyroxene and orthopyroxene and that clinopyroxene and orthopyroxene contribute 15% and 20%, respectively, to D_o , and 70% and 10%, respectively, to ϕ . In addition, we have assumed that clinopyroxene melts out of the residue at 30% melting, and therefore the abundances of Na₂O and TiO₂ in instantaneous melts produced by > 30% are given by $\sim 1/F$ for Na₂O and $1/(0.02+F(0.98))$ for TiO₂.

The polybaric melting path for each oxide gives the abundances of the oxide in instantaneous melts throughout the melting column ($C_i(F)$). If these instantaneous melts pool from throughout the column, the mean abundance of an oxide (\bar{C}_i) in the pooled melt is given by

$$\bar{C}_i = \left[\int_0^{F_f} C_i(F) * F dF \right] / \left[\int_0^{F_f} F dF \right] \quad (9)$$

where F_f is $0.012 * (P_o - P_f)$.

Major element compositions of pooled melts calculated as described above are shown in Table 3. Because the estimates of the polybaric melting paths require extrapolation back to 0% melting, the abundances of those oxides that show large changes in concentration at small extents of melting and show strong pressure dependencies are not well constrained; this is the case for SiO₂ (Figure 13) and for Al₂O₃. Given the scant experimental data and the resultant uncertainties involved in determining the polybaric melting paths for each oxide, we stress that the values presented in Table 3 should be viewed as estimates. We expect that the general trends for each oxide with changing P_o are correct but that further refinements on these calculations must await more detailed experiments on the melting behavior of peridotites.

The calculations above are based on the results of experimental studies performed primarily on spinel peridotites. More detailed experiments within the garnet peridotite facies are needed for evaluation of the melting systematics within the deepest parts of the melting column. *Presnall and Hoover* [1987] have pointed out that melting systematics in the plagioclase peridotite facies may differ significantly from those in the spinel peridotite facies. Furthermore, the melting behavior of Ca and, particularly, Al and Na may differ between plagioclase and spinel peridotite facies because these elements are the dominant constituents of plagioclase. The value of the percent melting per kilobar is unlikely to change substantially, however, because it is controlled primarily by the heat of fusion and heat capacity of the mantle minerals. Thus, for

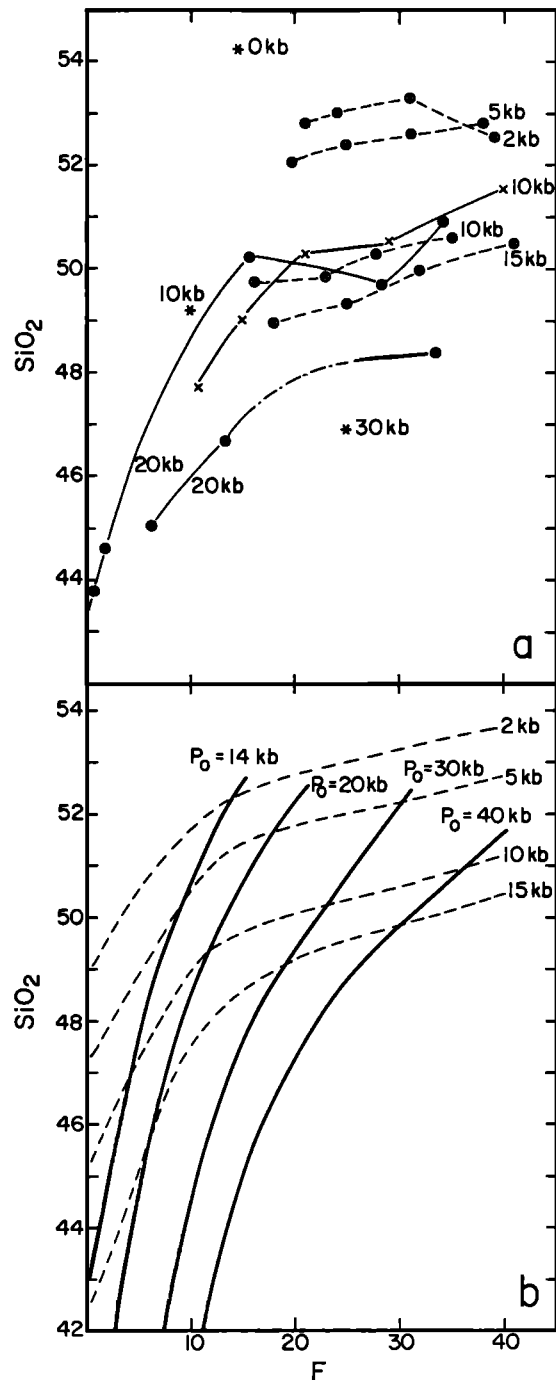


Fig. 13. SiO_2 (wt %) versus F (extent of melting). (a) Results of several experimental studies on the isobaric melting of various peridotitic compositions at the pressures indicated. Sources and starting compositions are: pyrolite (circled crosses), Tinaquillo lherzolite (crosses, only 10-kbar melts shown) [Jaques and Green, 1980]; garnet lherzolite \pm water (solid circles) [Mysen and Kushiro, 1977]; natural spinel lherzolite (asterisks; extents of melting estimated from reported Na_2O and TiO_2 abundances) [Takahashi, 1985]. (b) From the trends of the experimental data shown in Figure 13a, with particular emphasis on the pyrolite melting studies, isobaric melting curves (dashed) were estimated for 2, 5, 10, and 15 kbar. Assuming 1.2% melt/kbar pressure release, polybaric melting curves (solid) were estimated for P_0 of 40, 30, 20, and 14 kbar, by fitting to the isobaric melting curves (e.g., for $P_0=40$, 30% melting will be achieved by 15 kbar). The polybaric melting curves estimate the SiO_2 abundances in instantaneous melts present in the melting column at each pressure above the solidus ($C_i(F)$).

appropriate mantle compositions (5–10% aluminous phase), plagioclase is likely to be melted out of the residue by about 15% melting. If plagioclase becomes stable at 8–9 kbar, then for any value of P_0 greater than 20 kbar, the extent of melting achieved by the pressure of plagioclase stability is likely to equal or exceed the amount of melting where plagioclase may be a residual phase. Thus it is only for the very coolest regions (smallest extents of melting) that plagioclase may remain in the residue. A full evaluation of the importance of plagioclase must await experiments on appropriate mantle compositions in the plagioclase stability field.

Calculation of Crustal Thickness

Given the compositions in Table 3, it is possible to calculate crustal density, and hence convert crustal thickness in units of kilobars in equation (5) to a thickness in kilometers. To do this, the calculated crustal compositions in Table 3 were converted to normative minerals, and the known molar volumes and masses of these minerals were used to calculate crustal density. Crustal densities were plotted versus P_0 , and an empirical curve was fitted to the data. The mean density for the crust (ρ_c) produced by intersection of the solidus at a given P_0 is thus determined by the following empirical equation:

$$\rho_c = 2.6212 * P_0^{(0.038)} \quad (10)$$

Crustal thickness is then obtained from equation (A5) in the appendix. Note that these calculations predict a relationship between crustal chemistry and crustal thickness independent of the observational data. The calculations are compared to available data in Figure 14.

Figure 14 shows that the predicted inverse correlation exists between seismically determined estimates of crustal thickness and $\text{Na}_8.0$ for various regions encompassing the range of chemistry and bathymetry shown in Table 1.

TABLE 3. Calculated Pooled Melt Compositions and Other Physical Parameters for Varying Pressure of Intersection of the Solidus

	P_0			
	40 kbar	30 kbar	20 kbar	14 kbar
<i>Pooled Melt Compositions</i>				
SiO_2	48.50	49.03	49.85	50.40
Al_2O_3	12.70	14.20	15.20	16.40
FeO	9.53	8.80	8.22	7.70
MgO	15.10	13.60	11.80	10.20
CaO	11.10	11.90	11.30	9.90
Na_2O	1.31	1.61	2.13	2.70
TiO_2	0.72	0.88	1.14	1.40
Sum	99.0	100.0	99.6	98.7
Mg#	0.74	0.73	0.72	0.70
$\text{CaO}/\text{Al}_2\text{O}_3$	0.87	0.83	0.74	0.60
<i>Physical Parameters</i>				
\bar{F} , %	20.0	15.6	10.8	7.8
\bar{P} , kbar	16.4	11.7	7.3	4.9
D_c , km	22.5	13.8	6.8	3.6
D_w , km*	0	1.7	3.3	4.1

* Depth of compensation = 200 km.

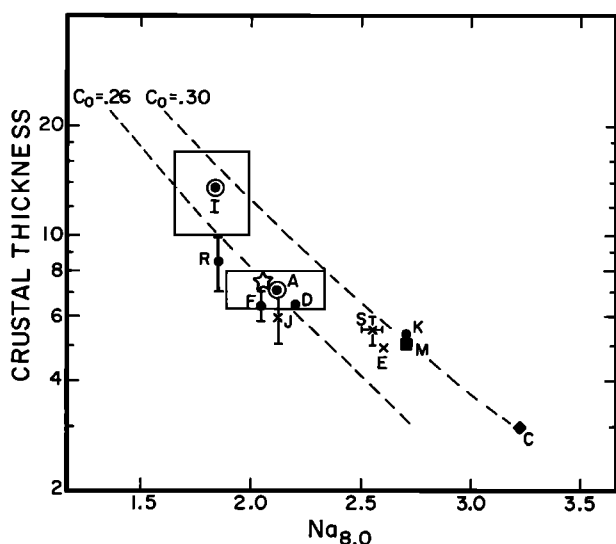


Fig. 14. Seismically determined estimates of crustal thickness versus $\text{Na}_{8.0}$ with the exception of the crustal thickness value for the Cayman Trough (C) which was estimated from geologic evidence. Data sources for crustal thickness are as follows: A (Azores region), Searle [1976]; C (Mid-Cayman Rise), Stroup and Fox [1981]; D (MAR at approximately 45°N), Lewis and Snyderman [1979]; F (MAR at approximately 37°N), Whitmarsh [1973] and Fowler [1976]; I (Iceland region), Palmason and Saemundsson [1974] and Bjornsson [1984]; J (Juan de Fuca), McClain and Lewis [1982]; K (MAR, Kane transform region), Detrick and Purdy [1980]; M (Mariana Trough), LaTraille and Hussong [1980]; R (Reykjanes Ridge), Bunch and Kennett [1980]; S (EPR near Siqueiros transform), Orcutt et al. [1976]. Values for $\text{Na}_{8.0}$ for each region are from Table 1. Where information on the range of crustal thickness estimates for a particular region were given, the range is included in the figure. The star is for samples from 140 m.y. crust from the western North Atlantic [Purdy, 1983; Byerly and Sinton, 1980]. Also shown are calculated curves for crustal thickness versus $\text{Na}_{8.0}$; crustal thickness is determined by equation (A5), and $\text{Na}_{8.0}$ values are derived by fractionation to 8 wt % MgO from the parental magma compositions in Table 3. The two curves correspond to different values of mantle Na_2O ($C_0=0.26$ or 0.30 wt %).

Although the slopes of the calculated curves are clearly consistent with the available data, the relative position of the curves is quite sensitive to the source abundance of Na_2O , as is shown. The best fit is for a source concentration of 0.26 wt % Na_2O , which is slightly less than primitive mantle abundances ($0.30 \text{ wt } \pm 0.03$), suggesting that the MORB mantle may be slightly depleted relative to bulk silicate mantle. It should also be noted that the calculated curves assume complete segregation of melt from throughout the melting column, and hence maximum crustal thickness. If some percentage of melt is retained within the residual matrix, as is likely, crustal thickness will decrease proportionately. To first order, however, the general correspondence of the data to the calculated curves of Figure 14 suggest that variations in the extent of melting and hence chemistry correspond with changes in the thickness of the oceanic crust.

Calculation of Relative Changes in Axial Depth

In the discussion above, variations in basalt chemistry were used to infer both variations in the thermal structure of the mantle underlying different spreading centers and in crustal thickness. Because the chemical variations also

correlate with axial depth, our findings have important implications for models of ridge axis bathymetry.

Contributions to average ridge axis bathymetry frequently discussed include variations in crustal thickness, mantle temperature, and mantle flow. The fact that $\text{Na}_{8.0}$ (and by inference, extent of melting) generally correlates with crustal thickness and with axial depth (Figure 2) supports geophysical models of ridge axis bathymetry which, to first order, call upon isostatic compensation of varying crustal thicknesses to account for variations in residual depth (see, e.g., review by Watts and Daly [1981]).

The model developed in the discussion, however, has several aspects in addition to crustal thickness which would contribute to axial depth. The observed variations in crustal thickness may result from temperature differences of as much as 250°C at equivalent depths in the subsolidus mantle. Since a column of mantle of higher mean temperature will be less dense, ridges underlain by higher mantle temperatures will be shallow simply due to thermal effects alone. In addition, hotter mantle starts melting deeper and creates a thicker mantle residue, and the mantle residue after melting is lighter than the fertile mantle prior to melting [e.g., Oxburgh and Parmentier, 1977]. It is therefore necessary to try to constrain the separate effects of variations in mantle temperature, residue thickness, and crustal thickness.

In the appendix, we have calculated the expected range in axial depth of isostatically balanced columns resulting from the coupled effects of variations in the extent of melting, crustal thickness, and mantle temperature. The results of the calculations are presented in Table 3 and Figure 15a, where the differences in water depth for specified P_0 's are expressed relative to an assumed water depth of zero for $P_0=40$ kbar. The relative changes in water depth also depend on the assumed depth of compensation (Figure 15a). For a compensation depth of 200 km and mean extents of melting between 8% and 20%, the total range in water depth is 4.1 km (Figures 15a and 15b). The effects of temperature variations alone on the calculated water depths can be determined by setting the coefficients of thermal expansion to zero in equations (A15) and (A17); the total range in water depth for 8-20% mean melting then becomes 3.2 km (Figure 15b). Thus temperature variations alone contribute approximately 1 km (<25%) to the total depth range. Further, we can examine the effect of variations in crustal thickness alone by assuming a mantle of constant temperature and density. The total range in water depth for 8-20% mean melting then is only 2.5 km. Thus variations in crustal thickness account for approximately half of the total depth range.

To compare calculated depths to observed depths, it is necessary to distinguish between axial depth, which includes the effects of rift valleys or axial highs, and regional depth. Figure 15a shows $\text{Na}_{8.0}$ plotted against ridge depth that has been averaged from zero-age to a 5 m.y. isochron, [Andrews et al., 1985; W. Haxby et al., manuscript in preparation, 1987]. Also plotted are calculated curves of relative variations in axial depth for compensation depths of 150, 200, and 250 km, as described above. The overall trend of the data agrees well with the calculated curves, but there are some discrepancies. In particular, most of the hot spot centers appear to be anomalously shallow, or anomalously high in Na_2O , compared to the calculated curves. Thus the

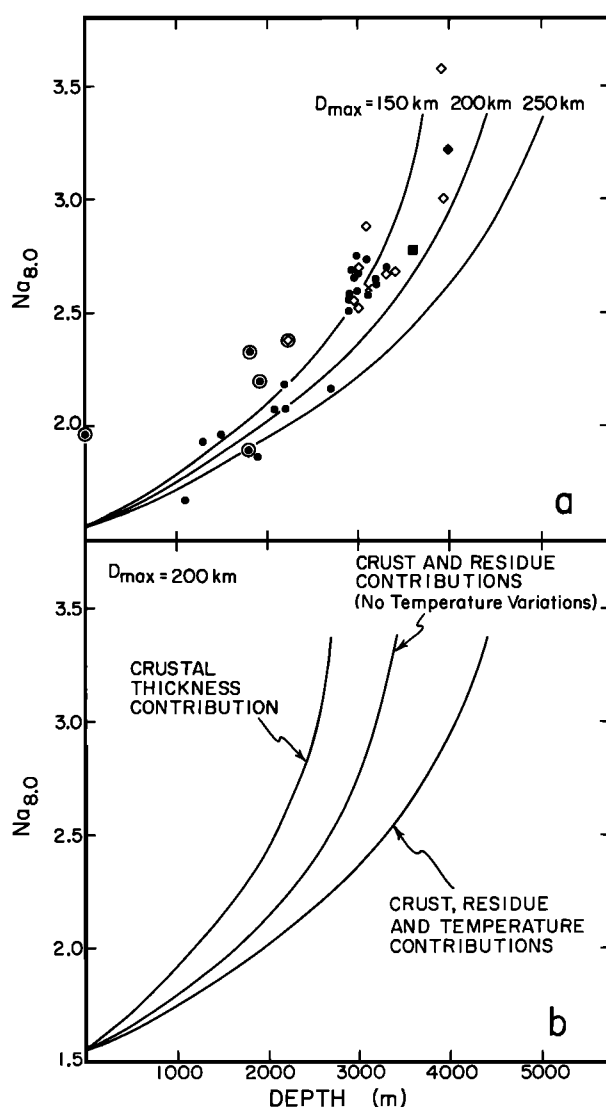


Fig. 15. (a) Data points show Na_2O from Table 1 versus ridge depth averaged to a 5 m.y. isochron; 5 m.y. average depths are predominantly from Andrews *et al.* [1985] and W. Haxby *et al.* (manuscript in preparation, 1987), supplemented with estimates from the data of Fryer and Hussong [1980], Stroup and Fox [1981], and the ROSE expedition (E. Vera, personal communication, 1987). Symbols as in Figure 2. Curves show Na_2O and depth variations calculated as described in the appendix for different depths of compensation (150, 200, or 250 km); Na_2O for the calculated curves are derived by fractionation from the compositions presented in Table 3. (b) Curves showing relative contributions to depth of the various parameters discussed in the appendix, for a compensation depth of 200 km. Curve labeled "crust, residue, and temperature contributions" is the same as the $D_{\text{max}} = 200 \text{ km}$ curve in Figure 15a; curve labeled "no temperature variations" is calculated by setting $\alpha = 0$ in equations (A15) and (A17). Curve labeled "crustal thickness contribution" is calculated assuming a constant mantle density of 3.34 gm/cm^3 .

sources for hot spot centers may either be slightly higher in Na_2O , or their anomalous depths may result from a component of mantle flow [e.g., Morgan, 1972; McKenzie *et al.*, 1974; Sclater *et al.*, 1975].

Comparison With Studies of Oceanic Ultramafic Rocks

As noted above, studies of oceanic peridotites [Dick *et al.*, 1984; Michael and Bonatti, 1985] are remarkably consistent

with the global correlations and inferences derived from them. Thus the results of this study strongly reinforce the methodology and conclusions of these previous studies. There are two aspects of the ultramafic data, however, which need further discussion for comparison between the peridotite and basalt data.

Both ultramafic studies were heavily influenced by samples recovered near the Azores platform. Langmuir and Hanson [1980] pointed out the anomalously low FeO of basalts from this region and suggested that this may result from a higher $\text{Mg}/(\text{Mg}+\text{Fe})$ ratio in the mantle source. MORB from the Azores region are also anomalous in the context of the global correlations (Figure 2). If the Azores region source had higher $\text{Mg}/(\text{Mg}+\text{Fe})$ to begin with, then the depletion in the ultramafics caused by melting would have been in addition to the preexisting depletion. This may in part explain the highly depleted ultramafics from this region.

The ultramafic samples, emplaced at crustal levels, also necessarily represent the residues of the very last increment of melt removed from the mantle. If the erupted melt is a mixture of melts from the entire melting zone, then parental ocean ridge basalts should not be in equilibrium with the sampled ultramafics. Instead, one might expect the ultramafics to be far more depleted than expected from normal MORB chemistry because the ultramafics may represent the end result of a continuous melting process [Bender *et al.*, 1984]. This complicates a direct connection between the peridotite and basalt data sets. The rarely observed, but often inferred, very depleted MORB end-member capable of crystallizing An₉₂ plagioclase may be a remnant of melts in equilibrium with the depleted peridotites at the top of the melting column.

Implications for the Compositions of Primary Magmas

Our calculations of the pooled melt compositions as a function of P_0 have important implications for the ongoing debate over the composition and equilibration pressure of primary MORB magmas. One group of experimentalists has argued for primary magmas equilibrated at pressures of greater than 15 kbar, and with MgO contents in excess of 14 wt %, and even in excess of 20 wt % [e.g., O'Hara, 1968; Elthon and Scarfe, 1984; Stolper, 1980]. Others have argued for an equilibration pressure of about 10 kbar and MgO contents of about 10 wt % [e.g., Presnall and Hoover, 1984, 1987; Fujii and Scarfe, 1985]. All of these works had as a paradigm a single pressure of equilibration for a particular primary magma and attempted to derive all MORB primary magmas from a restricted range in pressure.

A difficulty with the "constant pressure" paradigm is that it predicts that MORB primary magmas should be related by different extents of melting at a constant pressure. Instead, there appears to be a positive correlation between the extent and pressure of melting. This finding leads to a different perspective on primary magmas, where melts are generated in a polybaric melting column and where magmas seen at the surface are mixtures of melts from different pressures within the mantle melting column. Thus there may be no single "equilibration pressure" for any primary magma, and the mean equilibration pressure will vary as a function of the pressure of intersection of the solidus.

Furthermore, the fractionation-corrected basalt data and the partial melting calculations support the idea that there are

diverse primary magma compositions that can vary substantially in their major element composition and mean pressures of equilibration from region to region. Mean pressures, where half the melt is generated above and below that pressure, fall between approximately 5 and 16 kbar. The mean MgO content of eruptives varies between 10 and 15 wt %. On average, there should be an inverse correlation between the mean values of MgO (and pressure) and the depth of the spreading axis. This diversity of mean extents and pressures of melting and pooled melt compositions may in part explain the diverse points of view in the "primary magma" controversy. Indeed, several of the previous studies have used one or a few high MgO samples to represent MORB primary magmas. Since there appears to be a large range in MORB primary magma compositions, a perspective from any small number of samples, even the most primitive ones, will be incomplete.

It should also be noted that although one can define a mean pressure for the pooled melts, this mean pressure should not be confused with the isobaric "equilibration pressure" referred to in most experimental studies [e.g., Stolper, 1980]. The chemical composition of the pooled melt produced by a particular mean pressure and mean extent of melting does not correspond to the composition of the melt produced by melting to the same extent at a single pressure equal to the mean pressure. Thus, even if the isobaric melting paths on pseudo-phase diagrams were perfectly determined, the mean pressure of equilibration for pooled melts could not be determined from such information alone.

Last, we note that as melting proceeds in an ascending mantle column, a wide range of melt compositions are generated in the column. Thus there is the potential for the occasional eruption of magmas from substantially higher or lower pressures than the mean pressure. The global systematics of regional averages do not preclude the possibility of eruption of sporadic diverse and unusual compositions.

Spreading Rate

A remarkable feature of the global variations in major element chemistry is the lack of an obvious correlation with spreading rate. The slowest spreading ridges erupt both the highest and lowest Na₂O basalts, and have both the thickest and thinnest crust (Figure 14). These findings appear at first to conflict with the conclusions of Reid and Jackson [1981], who found that crustal thickness correlates with spreading rate. It should be noted, however, that Reid and Jackson regarded hot spots as anomalous and based their conclusions on "normal" ocean ridges. Although instances have been noted above where hot spot centers deviate from the global trends (see, e.g., Figures 2b and 2c), a fundamental finding presented herein is that many hot spots show the same relations between chemistry, depth, and crustal thickness as non-hot spot spreading centers (see, e.g., Figures 2a and 14).

However, it is clear that at very slow spreading rates, conductive cooling will affect the upwelling mantle, and the assumption of adiabatic ascent will no longer be valid [Bottinga and Allegre, 1978; Reid and Jackson, 1981]. This may be a partial explanation for the occurrence of thin crust at the slowest spreading rates, and under these conditions, provides a possible alternative to the "mantle temperature"

hypothesis presented above. It may be significant, however, that the fastest spreading ridges are all of average chemistry and depth, while the slowest spreading ridges can exhibit any depth or chemistry. This suggests that somehow the fastest ridges may be able to "damp out" the effects of extremes in temperature variations.

Implications for Studies of Older Crust and Temporal Variations in Mantle Temperature

The main results of this paper are the quantitative relationships among crustal thickness, basalt chemistry, and mantle temperature beneath the ridge. Such relationships should apply independent of age and thus may provide a tool for studying thermal variations beneath ocean ridges as a function of time.

The potential utility of this approach can be illustrated using crustal thickness data on 140 m.y. crust from the western Atlantic and comparing it with basalt chemical variations from Deep Sea Drilling Project legs 51-53 in the same general region (within 500 km) [Byerly and Sinton, 1980; Rice *et al.*, 1980]. The seismic data showed that the Cretaceous crust in this region is significantly thicker than zero-age crust on the Mid-Atlantic Ridge south of the Kane Fracture Zone, although the older crust lies approximately along a flow line emanating from the latter. The basalt data from this older crust show the chemical characteristics of moderately thick zero-age crust. The star symbols in Figures 8 and 14 show the chemical and crustal thickness data from this older region; these data are consistent with the zero-age chemical correlations. The data thus suggest that the thicker crust in this region is due to higher temperatures beneath the ridge in the Cretaceous than exist now at zero-age along the same flow line. An increase in crustal thickness by underplating, serpentinization or other age-dependent mechanisms is not required and indeed may be difficult to reconcile with the chemical data.

These results raise the possibility that temporal variations in mantle temperature beneath the ridge can be studied by multichannel seismic profiling of older crust or by chemical sampling. Further evidence of the correlation between regional crustal thickness and basalt chemistry, however, must be obtained by additional drilling with complementary seismic experiments.

CONCLUSIONS

Examination of a global data base shows that there are systematic global variations in basalt chemistry that correlate with axial depth. Shallow regions, such as the Kolbeinsey ridge, show the following characteristics: high CaO, low Al₂O₃ (high CaO/Al₂O₃), low Na₂O, high FeO, low SiO₂, high Sc, low Sm/Yb, and low Ni. In contrast, basalts from deep regions such as the Australian-Antarctic Discordance or Mid-Cayman Rise, show the opposite chemical trends. Between these shallow and deep end-members, a continuum of compositions is observed. The observed chemical systematics are remarkably consistent with the results of experimental studies on the melting of peridotitic compositions and with compatible trace element modeling, suggesting that basalts occurring on shallow ridge segments are derived by larger extents of melting at greater mean pressures of melt segregation. More extensive experimental data are needed, however, to test this possibility rigorously. Some hot spots (e.g., Azores, Jan

Mayen, Galapagos) appear to be chemically anomalous in a global context and may represent evidence of major element source heterogeneity.

Calculations based on the chemistry of the end-member basalt compositions suggest that the mean extents of melting range from approximately 8 to 20% and the mean pressures of melting range from 5 to 16 kbar. Calculated crustal thicknesses produced by this range in extent of melting are consistent with those inferred from seismic studies. These calculations also suggest that between the end-member basalt compositions, temperature differences in the sub-solidus mantle may be as much as 250°C.

Calculations of predicted depth ranges depend on the depth of isostatic compensation, crustal thickness, residue thickness, and mantle temperature. For a compensation depth of 150–200 km, the relative depth changes for the isostatic model are consistent with observed depths, but some hot spot centers may be anomalously shallow, or alternatively their sources may be anomalously high in Na₂O.

Thus there appears to be consistency among three of the major observable features of the global system of ocean ridges, chemical composition, crustal thickness, and water depth, all of which are diverse manifestations of the temperature variations in the mantle. This apparent consistency needs to be tested by further sampling of areas that show substantial zero-age depth and crustal thickness variations. The same principles relating chemistry and crustal thickness should also apply to older ocean crust, which raises the possibility of petrologically constraining the origins of bathymetric anomalies throughout the ocean basins.

APPENDIX

In the following, we present a method for calculating differences in water depth between isostatically balanced unit columns extending to a specified depth of compensation, D_{max} , as a function of mantle temperature differences. Each column consists of water, crust, residual mantle that has melted to produce the crust, and fertile mantle extending from the base of the residual mantle to D_{max} (Figure A1). Thus the total mass for each column, M_T , is

$$M_T = \rho_w D_w + \rho_c D_c + \rho_r D_r + \rho_m D_m \quad (A1)$$

and the total column height to D_{max} is

$$D_{max} = D_w + D_c + D_r + D_m \quad (A2)$$

where subscripts w , c , r , and m refer to water, crust, residual mantle, and fertile mantle, respectively, and ρ and D refer to density and thickness. The densities and thicknesses of the components of each column will vary with composition, temperature, and pressure. Each of these are controlled by the mantle temperature prior to crust formation, since mantle temperature controls the pressure and temperature of intersection of the solidus and hence the thickness and composition of both crust and residue. In the following, relative differences in water depth (D_w) are calculated as a function of differences in mantle temperature beneath the ridge.

Temperature differences control the pressure at which melting begins in an upwelling mantle diapir. The temperature T_0 and pressure P_0 at which melting begins are related by an equation approximating the mantle solidus

[Takahashi and Kushiro, 1983]:

$$T_0 = 1150^\circ\text{C} + 12^\circ\text{C/kb} * P_0 \quad (A3)$$

T_0 and P_0 control the extent of melting and hence the resulting melt composition, assuming a homogeneous mantle. Calculated melt compositions, presented in Table 3, can be used to calculate crustal densities by determining molecular norms and then applying the partial molar volumes for the normative minerals [e.g., Robie *et al.*, 1979] to calculate densities. An empirical equation for the calculated crustal densities as a function of P_0 , which recovers values to better than 0.1% within the range of basalt compositions considered, is

$$\rho_c = 2.6212 * P_0^{(0.038)} \quad (A4)$$

Crustal thickness, D_c , described by equation (8) in the text, is in units of kilobars. Conversion to kilometers can be accomplished by using the density from equation (A4) and the fact that 1020 g/cm³ is equivalent to 1 bar at the earth's surface. Then, allowing for conversion from bars to kilobars and centimeters to kilometers, D_c , in kilometers, is

$$D_c = 0.006 * (P_0 - P_f)^2 * 10.2/\rho_c \quad (A5)$$

The residual mantle is that portion of the mantle between the initial (P_0) and final (P_f) pressures of melting. The density of the residual mantle varies with pressure, temperature, composition, and mineralogy. The effects of the latter two parameters can be modeled as a function of the extent of melting. We take the 1 atm, 25°C densities of fertile plagioclase lherzolite and garnet-spinel lherzolite to be 3.27 g/cm³ and 3.34 g/cm³, respectively. The boundary between plagioclase and spinel lherzolite is taken to be 8 kbar [Presnall *et al.*, 1979]. Density of the mantle is assumed to vary linearly as the fraction of melting ($F=0.012*\Delta P$) increases from 0 to 0.3, between the initial value for unmelted mantle and a value of 3.295 g/cm³ for residual harzburgite [Oxburgh and Parmentier, 1977]; when F exceeds 0.3, density is maintained at 3.295 g/cm³. Thus a different density is calculated for each facies depending on the mean fraction of melting that occurs within that facies. The mean fractions of melting within plagioclase and garnet-spinel facies (subscripts pl or $gt-sp$) are controlled by P_0 and P_f , analogous to equation (6), and are given by

$$\overline{F}_{pl} = 0.006 * (2P_0 - P_f - 8) \quad (A6)$$

$$\overline{F}_{gt-sp} = 0.006 * (P_0 - 8) \quad (A7)$$

Then, the 1 atm, 25°C densities (denoted by primed superscripts) within each facies can be calculated as a function of the mean extents of melting within each facies:

$$\rho'_{pl} = 3.27 + \overline{F}_{pl} * [(3.295-3.27)/0.3] \quad (A8)$$

$$\rho'_{gt-sp} = 3.34 + \overline{F}_{gt-sp} * [(3.295-3.34)/0.3] \quad (A9)$$

provided F is less than 0.3, with a value for ρ' of 3.295 integrated into the result for those portions where F exceeds 0.3. Thicknesses of residual mantle within each facies can be determined, as in (A5), ignoring the slight change in the earth's gravitational field with depth over the depth range considered:

$$D_{pl} = (8 - P_f) * (10.2/\rho'_{pl}) \quad (A10)$$

$$D_{gt-sp} = (P_0 - 8) * (10.2/\rho'_{gt-sp}) \quad (A11)$$

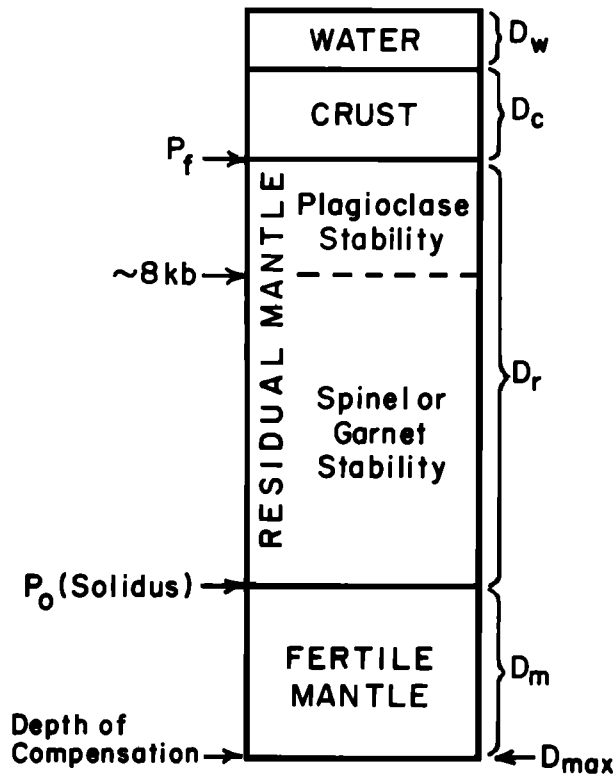


Fig. A1. Schematic representation of isostatically balanced columns, consisting of fertile mantle, residual mantle, crust, and water, as discussed in the text.

The mean density of the residual mantle at 1 atm and 25°C is then given by the relative contributions within each facies:

$$\rho'_r = [D_{pl}/(D_{pl} + D_{gt-sp})] * \rho'_{pl} + [D_{gt-sp}/(D_{pl} + D_{gt-sp})] * \rho'_{gt-sp} \quad (\text{A12})$$

The mean in situ density of the residual mantle depends on the mean temperature and pressure of the residual mantle. Assuming that pressure decreases linearly between P_0 and P_f , mean pressure in the residual mantle is given by

$$P_r = (P_0 + P_f)/2 \quad (\text{A13})$$

Mean temperature depends on T_0 and the temperature decrease that occurs through melting by adiabatic decompression, which we take to be approximately 6°C/kbar [Cawthorn, 1975]. Mean temperature in the residual mantle is then given by

$$T_r = [T_0 + T_0 - 6^\circ\text{C/kb} * (P_0 - P_f)]/2 = T_0 - 3(P_0 - P_f) \quad (\text{A14})$$

Using values of $3 \times 10^{-5}/^\circ\text{C}$ and $10^{-3}/\text{kbar}$ for the volume coefficients of thermal expansion (α) and compressibility (β) [Birch, 1952], the mean density of the residual mantle is given by

$$\rho_r = \rho'_r * [1 - \alpha * (T_r - 25^\circ\text{C}) + \beta * P_r] \quad (\text{A15})$$

The thickness of the residual mantle, as in (A5), is then given by

$$D_r = (P_0 - P_f) * 10.2 / \rho_r \quad (\text{A16})$$

The mean density of the fertile mantle at 1 atm and 25°C

is taken as that of spinel or garnet lherzolite (3.34 g/cm³). As in (A15), the mean in situ density of the fertile mantle depends on the mean temperature (T_m) and pressure (P_m) of the fertile mantle:

$$\rho_m = 3.34 * [1 - \alpha * (T_m - 25^\circ\text{C}) + \beta * P_m] \quad (\text{A17})$$

For a given maximum depth of compensation (D_{max}), the mean pressure of the fertile mantle (P_m) is given by the difference in pressure between that at D_{max} (P_{max}) and the pressure where melting begins, P_0 :

$$P_m = (P_{max} + P_0)/2 \quad (\text{A18})$$

The mean temperature of the fertile mantle (T_m) is given by T_0 and the adiabatic gradient from P_0 to P_{max} :

$$T_m = T_0 + 2^\circ\text{C/kb} * [(P_{max} - P_0)/2] \quad (\text{A19})$$

Equations (A17)-(A19) can be evaluated once P_{max} is determined. P_{max} , in turn, depends upon a knowledge of the total column mass M_T . If, however, we specify that for a particular P_0 (taken as 40 kbar), water depth (D_w) is zero, then for this P_0 , the thickness of the fertile mantle, from equation (A2), is

$$D_m = D_{max} - D_r - D_c \quad (\text{A20})$$

since $D_w=0$ for $P_0=40$ kbar. Total column mass and pressure at D_{max} can then be determined iteratively. Using an initial, arbitrary value for ρ_m (e.g., 3.34 g/cm³) and equations (A1) and (A3)-(A16), M_T and P_{max} ($=M_T/10.2$) are calculated; P_{max} is then used to recalculate ρ_m using equations (A1) and (A3)-(A16), and new values of M_T and P_{max} are determined. These calculations are repeated until convergence is obtained for both M_T and P_{max} .

Because M_T and P_{max} are constant for each isostatically balanced column independent of variations in P_0 , water depth can be calculated for all other specified P_0 's using equations (A1)-(A19). The results of these calculations, presented in Table 3 and Figure 15a, thus provide differences in water depth and crustal thickness as a function of mantle temperature and depth of compensation.

Acknowledgments. The authors are indebted to the following people for generously giving of their thoughts and expertise: D. Walker, R. Buck, C. Lesher, J. Bender, A. Watts, J. Andrews, W. Haxby, J. Natland, B. Parsons, W. Ryan, D. Fornari, E. Bonatti, K. Kastens, N. Bogen, L. Cathles, L. Viereck, T. Plank, and Y. Zhang. Formal reviews by B. Hager, D. Presnall, and J. Sinton contributed greatly to the substance and clarity of the manuscript. Discussions with D. Christie were very helpful in understanding the systematics of mantle melting. In addition, a Saturday discussion with D. McKenzie during the final stages of preparation of the submitted version of this manuscript was both enjoyable and illuminating. We are also indebted to R. Glynn for suffering multiple revisions, and to P. Catanzaro for her careful drafting of the figures. This work was supported by National Science Foundation grants OCE84-11448 and OCE86-16484. Lamont-Doherty Geological Observatory Contribution 4135.

REFERENCES

- Ahern, J.L., and D.L. Turcotte, Magma migration beneath an ocean ridge, *Earth Planet. Sci. Lett.*, **45**, 115-122, 1979.
Andrews, J.A., W.F. Haxby, and W.R. Buck, Variations in geoid

- height-age relationships over young oceanic lithosphere, *Eos Trans. AGU*, 66, 846, 1985.
- Barker, P.F., A spreading center in the east Scotia Sea, *Earth Planet. Sci. Lett.*, 15, 123-132, 1972.
- Bender, J.F., F.N. Hodges, and A.E. Bence, Petrogenesis of basalts from the Project FAMOUS area: Experimental study from 0 to 15 Kbars, *Earth Planet. Sci. Lett.*, 41, 277-302, 1978.
- Bender, J.F., C.H. Langmuir, and G.N. Hanson, Petrogenesis of basalt glasses from the Tamayo region, East Pacific Rise, *J. Petrol.*, 25, 213-254, 1984.
- Birch, F., Elasticity and constitution of the earth's interior, *J. Geophys. Res.*, 57, 227-286, 1952.
- Bjornsson, S., Crust and upper mantle beneath Iceland, Structure and Development of the Greenland-Scotland Ridge, edited by M.H.P. Bott, S. Saxov and M. Talwani, 4 (8), 31-61, NATO Conf. Ser., 1984.
- Bonatti, E., P. Colantoni, B. Della Vedova, and M. Taviani, Geology of the Red Sea transitional region 22°N-25°N, *Oceanol. Acta*, 7, 385-398, 1984.
- Bottinga, Y., and C.J. Allegre, Partial melting under spreading ridges, *Philos. Trans. R. Soc. London, Ser. A*, 288, 501-525, 1978.
- Bryan, W.B., and H.J.B. Dick, Contrasted abyssal basalt liquidus trends: Evidence for mantle major element heterogeneity, *Earth Planet. Sci. Lett.*, 58, 15-26, 1982.
- Bryan, W.B., G. Thompson, and J.L. Ludden, Compositional variation in normal MORB from 22°-25°N: Mid-Atlantic Ridge and Kane Fracture Zone, *J. Geophys. Res.*, 86, 11,815-11,836, 1981.
- Bunch, A.W.H., and B.L.N. Kennett, The crustal structure of the Reykjanes Ridge at 59°30'N, *Geophys. J. R. Astron. Soc.*, 61, 141-166, 1980.
- Byerly, G.R., and J.M. Sinton, Compositional trends in natural basaltic glasses from Deep Sea Drilling Project holes 417D and 418D, *Initial Rep. Deep Sea Drill. Proj.*, 51-53, part 2, 957-971, 1980.
- Cawthorn, R.G., Degrees of melting in mantle diapirs and the origin of ultrabasic liquids, *Earth Planet. Sci. Lett.*, 27, 113-120, 1975.
- Christie, D.M., and J.M. Sinton, Evolution of abyssal lavas along propagating segments of the Galapagos Spreading Center, *Earth Planet. Sci. Lett.*, 56, 321-335, 1981.
- Detrick, R.S., and G.M. Purdy, The crustal structure of the Kane Fracture Zone from seismic refraction studies, *J. Geophys. Res.*, 85, 3759-3777, 1980.
- Dick, H.J.B., R.L. Fisher, and W.B. Bryan, Mineralogic variability of the uppermost mantle along mid-ocean ridges, *Earth Planet. Sci. Lett.*, 69, 88-106, 1984.
- Dickey, J.S., Jr., F.A. Frey, S.R. Hart, and E.B. Watson, Geochemistry and petrology of dredged basalts from the Bouvet triple junction, South Atlantic, *Geochim. Cosmochim. Acta*, 41, 1105-1118, 1977.
- Dungan, M.A., and J.M. Rhodes, Residual glasses and melt inclusions in basalts from DSDP legs 45 and 46: Evidence for magma mixing, *Contrib. Mineral. Petrol.*, 67, 417-431, 1978.
- Elthon, D., and C.M. Scarfe, High-pressure phase equilibria of a high-magnesian basalt and the genesis of primary oceanic basalts, *Am. Mineral.*, 69, 1-15, 1984.
- Fisher, R.L., J.G. Sclater, and D.P. McKenzie, Evolution of the Central Indian Ridge, western Indian Ocean, *Geol. Soc. Am. Bull.*, 82, 553-562, 1971.
- Fowler, C.M.R., Crustal structure of the Mid-Atlantic Ridge crest at 37°N, *Geophys. J. R. Astron. Soc.*, 47, 459-491, 1976.
- Fowler, C.M.R., and C.E. Keen, Oceanic crustal structure--Mid-Atlantic Ridge at 45°N, *Geophys. J. R. Astron. Soc.*, 56, 219-226, 1979.
- Frey, F.A., C.-Y. Suen, and H.W. Stockman, The Rhonda high temperature peridotite: Geochemistry and petrogenesis, *Geochim. Cosmochim. Acta*, 49, 2469-2491, 1985.
- Fryer, P., and D.M. Hussong, Seafloor spreading in the Mariana trough: Results of leg 60 drill site surveys, Deep Sea Drilling Project, *Initial Rep. Deep Sea Drill. Proj.*, 60, 45-55, 1981.
- Fryer, P., J.M. Sinton, and J.A. Philpotts, Basaltic glasses from the Mariana Trough, *Initial Rep. Deep Sea Drill. Proj.*, 60, 601-609, 1981.
- Fujii, T., and C.M. Scarfe, Composition of liquids coexisting with spinel ilherzolite at 10 kbar and the genesis of MORBs, *Contrib. Mineral. Petrol.*, 90, 18-28, 1985.
- Grove, T.L., and W.B. Bryan, Fractionation of pyroxene-phyric MORB at low pressure: An experimental study, *Contrib. Mineral. Petrol.*, 84, 293-309, 1983.
- Hamelin, B., B. Dupre, and C.J. Allegre, Lead-strontium isotopic variations along the East Pacific Rise and the Mid-Atlantic Ridge: A comparative study, *Earth Planet. Sci. Lett.*, 67, 340-350, 1984.
- Hart, S.R., and K.E. Davis, Nickel partitioning between olivine and silicate melt, *Earth Planet. Sci. Lett.*, 40, 203-219, 1978.
- Hart, S.R. and A. Zindler, In search of bulk earth composition, *Chem. Geol.*, in press, 1987.
- Hart, S.R., J.-G. Schilling, and J.L. Powell, Basalts from Iceland and along the Reykjanes Ridge: Sr isotope geochemistry, *Nature Phys. Sci.*, 246, 104-107, 1973.
- Hawkins, J.W., Jr., Petrology and geochemistry of basaltic rocks of the Lau Basin, *Earth Planet. Sci. Lett.*, 28, 283, 1976.
- Hayes, D.E., and J.R. Conolly, Morphology of the southeast Indian Ocean, in *Antarctic Oceanology, II, The Australian-New Zealand Sector, Antarct. Res. Ser.*, vol. 19, edited by D.E. Hayes, pp. 147-164, AGU, Washington, D. C., 1972.
- Henderson, P., *Inorganic Geochemistry*, 353 pp., Pergamon, New York, 1982.
- Hey, R.N., D.F. Naar, M.C. Kleinrock, W.J. Phipps Morgan, E. Morales, and J.-G. Schilling, Microplate tectonics along a superfast seafloor spreading system near Easter Island, *Nature*, 317, 320-325, 1985.
- Humphris, S.E., G. Thompson, J.-G. Schilling, and R.H. Kingsley, Petrological and geochemical variations along the Mid-Atlantic Ridge between 46°S and 32°S: Influence of the Tristan de Cunha mantle plume, *Geochim. Cosmochim. Acta*, 49, 1445-1464, 1985.
- Irving, A.J., A review of experimental studies of crystal/liquid trace element partitioning, *Geochim. Cosmochim. Acta*, 42, 743-770, 1978.
- Jagoutz, E., H. Palme, H. Baddenhausen, K. Blum, M. Cendales, G. Dreibus, S. Spettel, V. Lorenz, and H. Wanke, The abundances of major, minor and trace elements in the earth's primitive mantle as derived from primitive ultramafic nodules, *Proc. Lunar Planet. Sci. Conf.*, 10th, 2031-2050, 1979.
- Jaques, A.L., and D.H. Green, Anhydrous melting of peridotite at 0-15 kb pressure and the genesis of tholeiitic basalts, *Contrib. Mineral. Petrol.*, 73, 287-310, 1980.
- Kappel, E.S., and W.B.F. Ryan, Volcanic episodicity and a non-steady state rift valley along northeast Pacific spreading centers: Evidence from Sea MARC I, *J. Geophys. Res.*, 91, 13,925-13,940, 1986.
- Kay, R.W., N.J. Hubbard, and P.W. Gast, Chemical characteristics and origin of ocean ridge volcanic rocks, *J. Geophys. Res.*, 75, 1585-1613, 1970.
- Klein, E.M., C.H. Langmuir, A. Zindler, and H. Staudigel, Tectonic controls on major element, trace element and radiogenic isotopic compositions of Southeast Indian Ridge (SEIR) basalts; 115°E-138°E, *Eos Trans. AGU*, 65, 301, 1984.
- Klitgord, K.D., and J. Mammerrickx, East Pacific Rise: Magnetic anomaly and bathymetric framework, *J. Geophys. Res.*, 87, 6725-6750, 1982.
- Langmuir, C.H., and J.F. Bender, The geochemistry of oceanic basalts in the vicinity of transform faults: Observations and implications, *Earth Planet. Sci. Lett.*, 69, 107-127, 1984.
- Langmuir, C.H., and G.N. Hanson, An evaluation of major element heterogeneity in the mantle sources of basalts, *Philos. Trans. R. Soc. London, Ser. A*, 297, 383-407, 1980.
- Langmuir, C.H., J.F. Bender, A.E. Bence, G.N. Hanson, and S.R. Taylor, Petrogenesis of basalts from the FAMOUS area: Mid-Atlantic Ridge, *Earth Planet. Sci. Lett.*, 36, 133-156, 1977.
- Langmuir, C.H., J.F. Bender, and R. Batiza, Petrological and tectonic segmentation of the East Pacific Rise, 5°30'-14°30'N, *Nature*, 332, 422-429, 1986.
- LaTraille, S.L., and D.M. Hussong, Crustal structure across the Mariana Island arc, in *The Tectonic and Geological Evolution of Southeast Asian Seas and Islands*, Part 1, *Geophys. Monogr. Ser.*, vol. 23, edited by D.E. Hayes, pp. 209-222, AGU, Washington, D.C., 1980.
- Lawver, L.A., and H.J.B. Dick, The American-Antarctic Ridge, *J. Geophys. Res.*, 88, 8193-8202, 1983.
- Le Douaran, S., and J. Francheteau, Axial depth anomalies from 10° to 50° north along the Mid-Atlantic Ridge: Correlation with other mantle properties, *Earth Planet. Sci. Lett.*, 54, 29-47, 1981.

- leRoex, A.P., H.J.B. Dick, A.J. Erlank, A.M. Reid, F.A. Frey, and S.R. Hart, Geochemistry, mineralogy and petrogenesis of lavas erupted along the Southwest Indian Ridge between the Bouvet Triple Junction and 11 degrees east, *J. Petrol.*, **24**, 213-318, 1983.
- leRoex, A.P., H.J.B. Dick, A.M. Reid, F.A. Frey, A.J. Erlank, and S.R. Hart, Petrology and geochemistry of basalts from the American-Antarctic Ridge, Southern Ocean: Implications for the westward influence of the Bouvet mantle plume, *Contrib. Mineral. Petrol.*, **90**, 367-380, 1985.
- Lewis, B.T.R., and W.E. Snijders, Fine structure of the lower oceanic crust on the Cocos plate, *Tectonophysics*, **55**, 87-105, 1979.
- Macdonald, K. J.-C. Sempere and P.J. Fox, East Pacific Rise from Siqueiros to Orozco Fracture Zones: along-strike continuity of axial neo-volcanic zone and structure and evolution of overlapping spreading centers, *J. Geophys. Res.*, **89**, 6049-6069, 1984.
- McClain, K.J., and B.T.R. Lewis, Geophysical evidence for the absence of a crustal magma chamber under the northern Juan de Fuca Ridge: A contrast with ROSE results, *J. Geophys. Res.*, **87**, 8477-8489, 1982.
- McKenzie, D., The generation and compaction of partially molten rock, *J. Petrol.*, **25**, 713-765, 1984.
- McKenzie, D., The extraction of magma from the crust and mantle, *Earth Planet. Sci. Lett.*, **74**, 81-91, 1985.
- McKenzie, D.P., and J.G. Sclater, The evolution of the Indian Ocean since the Late Cretaceous, *Geophys. J. R. Astron. Soc.*, **24**, 437-528, 1971.
- McKenzie, D.P., J.M. Roberts, and N.O. Weiss, Convection in the earth's mantle: Towards a numerical simulation, *J. Fluid Mech.*, **62**, 465-538, 1974.
- Melson, W.G., and T. O'Hearn, Basaltic glass erupted along the mid-Atlantic ridge between 0-37°N: Relationships between composition and latitude, in *Deep Sea Drill Results in the Atlantic Ocean: Ocean Crust*, Maurice Ewing Ser., vol. 2, edited by M. Talwani, C.G. Harrison, and D.E. Hayes, pp. 249-261, AGU, Washington, D. C., 1979.
- Melson, W.G., and T. O'Hearn, "Zero-age" variations in the composition of abyssal volcanic rocks along the axial zone of the Mid-Atlantic ridge, in *The Geology of North America*, edited by P.R. Vogt and B.E. Tucholke, pp. 117-136, Geological Society of America, Boulder, Colo., 1986.
- Melson, W.G., T.L. Vallier, T.L. Wright, G. Byerly, and J. Nelsen, Chemical diversity of abyssal volcanic glass erupted along Pacific, Atlantic, and Indian Ocean seafloor spreading centers, in *The Geophysics of the Pacific Ocean Basin and Its Margin*, *Geophys. Monogr. Ser.*, vol. 19, edited by G.H. Sutton et al., pp. 351-367, AGU, Washington, D. C., 1976.
- Melson, W.G., G.R. Byerly, J.A. Nelsen, T. O'Hearn, T.L. Wright, and T. Vallier, A catalog of the major element chemistry of abyssal volcanic glasses, *Smithson. Contrib. Earth Sci.*, **19**, 31-60, 1977.
- Michael, P.J., and E. Bonatti, Peridotite composition from the North Atlantic: Regional and tectonic variations and implications for partial melting, *Earth Planet. Sci. Lett.*, **73**, 91-104, 1985.
- Morgan, W.J., Deep mantle convection plumes and plate motions, *Am. Assoc. Pet. Geol. Bull.*, **56**, 203-213, 1972.
- Mysen, B.O., and I. Kushiro, Compositional variations of coexisting phases with degree of melting of peridotite in the upper mantle, *Am. Mineral.*, **62**, 843-856, 1977.
- Nabelek, P.I., and C.H. Langmuir, The significance of unusual zoning in olivines from FAMOUS area basalt 527-1-1, *Contrib. Mineral. Petrol.*, **93**, 1-8, 1986.
- Neumann, E.-R., and J.-G. Schilling, Petrology of basalts from the Mohs-Knipovich Ridge: The Norwegian-Greenland Sea, *Contrib. Mineral. Petrol.*, **85**, 209-223, 1984.
- O'Hara, M.J., Are any ocean floor basalts primary magma?, *Nature*, **220**, 683-686, 1968.
- O'Hara, M.J., Importance of the "shape" of the melting regime during partial melting of the mantle, *Nature*, **314**, 58-62, 1985.
- Orcutt, J.A., B.L.N. Kennett, and L.M. Dorman, Structure of the East Pacific Rise from an ocean bottom seismometer survey, *Geophys. J. R. Astron. Soc.*, **45**, 305-320, 1976.
- Oxburgh, E.R., and E.M. Parmentier, Compositional and density stratification in oceanic lithosphere—Causes and consequences, *J. Geol. Soc., London*, **133**, 343-355, 1977.
- Palmason, G., and K. Saemundsson, Iceland in relation to the Mid-Atlantic Ridge, *Annu. Rev. Earth Planet. Sci.*, **2**, 25-50, 1974.
- Parsons, B., and S. Daly, The relationship between surface topography, gravity anomalies and temperature structure of convection, *J. Geophys. Res.*, **88**, 1129-1144, 1983.
- Perfit, M.R., C.H. Langmuir, M. Baekisapa, B. Chappell, R.W. Johnson, H. Staudigel, and S.R. Taylor, Geochemistry and petrology of volcanic rocks from the Woodlark Basin: Addressing questions of ridge subduction, *Marine Geology, Geophysics, and Geochemistry of the Woodlark Basin-Solomon Islands*, edited by B. Taylor and N. Exon, *Circum-Pacific Council for Energy and Mineral Resources, Earth Sci. Ser.*, Houston, Tex., in press, 1987.
- Phillips, J.D., and H.S. Fleming, Multibeam sonar study of the Mid-Atlantic Ridge rift valley, 36°N-37°N, *Geol. Soc. Am. Map Ser.*, MC-19, 1978.
- Pockalny, R., R. Detrick, and P.J. Fox, A Sea Beam map of the Kane transform: Implications for the tectonics of slowly-slipping transforms, *Eos Trans. AGU*, **66**, 1092, 1985.
- Presnall, D.C., and J.D. Hoover, Composition and depth of origin of primary mid-ocean ridge basalts, *Contrib. Mineral. Petrol.*, **87**, 170-178, 1984.
- Presnall, D.C., and J.D. Hoover, High pressure phase equilibrium constraints on the origin of mid-ocean ridge basalts, *Geochim. Cosmochim. Acta*, in press, 1987.
- Presnall, D.C., and T.H. O'Donnell, Origin of basalts from 25°-29°N on the Mid-Atlantic Ridge, *Eos Trans. AGU*, **57**, 341, 1976.
- Presnall, D.C., J.R. Dixon, T.H. O'Donnell, and S.A. Dixon, Generation of mid-ocean ridge tholeiites, *J. Petrol.*, **20**, 3-35, 1979.
- Price, R.C., A.K. Kennedy, M.R. Riggs-Sneeringer, and F.A. Frey, Geochemistry of basalts from the west Indian triple junction: Implications for the generation and evolution of Indian Ocean Ridge basalts, *Earth Planet. Sci. Lett.*, **78**, 379-396, 1986.
- Purdy, G.M., The seismic structure of 140 Myr old crust in the western central Atlantic Ocean, *Geophys. J. R. Astron. Soc.*, **72**, 115-137, 1983.
- Rice, S., C.H. Langmuir, J.F. Bender, G.N. Hanson, A.E. Bence, and S.R. Taylor, Basalts from Deep Sea Drilling Project holes 417A and 417D, fractionated melts of a light rare-earth depleted source, *Initial Rep. Deep Sea Drill. Proj.*, **51-53**, part 2, 1099-1110, 1980.
- Robie, R.A., B.S. Hemingway, and J.R. Fisher, Thermodynamic properties of minerals and related substances at 298.15K and 1 bar (10⁵ pascals) pressure and at higher temperatures, *U.S. Geol. Surv. Bull.*, **1452**, 12-29, 1979.
- Saunders, A.D., and J. Tarney, The geochemistry of basalts from a back-arc spreading centre in the East Scotia Sea, *Geochim. Cosmochim. Acta*, **43**, 555-572, 1979.
- Schilling, J.-G., Red Sea floor origin: Rare-earth evidence, *Science*, **165**, 1357-1360, 1969.
- Schilling, J.-G., Iceland mantle plume: Geochemical study of Reykjanes Ridge, *Nature*, **242**, 565-571, 1972.
- Schilling, J.-G., R.H. Kingsley, and J.D. Devine, Galapagos hot-spot-spreading center system, I. Spatial petrologic and geochemical variations, 83°W-101°W, *J. Geophys. Res.*, **87**, 5593-5610, 1982.
- Schilling, J.-G., M. Zajac, R. Evans, T. Johnston, W. White, J.D. Devine, and R. Kingsley, Petrologic and geochemical variations along the Mid-Atlantic Ridge from 29°N to 73°N, *Am. J. Sci.*, **283**, 510-586, 1983.
- Schilling, J.-G., H. Sigurdsson, A.N. Davis, and R.N. Hey, Easter microplate evolution, *Nature*, **317**, 325-331, 1985.
- Sclater, J.G., L.A. Lawver, and B. Parsons, Comparison of long-wavelength residual elevation and free air gravity anomalies in the North Atlantic and possible implications for the thickness of the lithospheric plate, *J. Geophys. Res.*, **88**, 1031-1052, 1975.
- Sclater, J.G., C. Brown, R. Hey, H. Hoskins, J. Peirce, J. Phillips, and C. Tapscott, The Bouvet Triple Junction, *J. Geophys. Res.*, **81**, 1857-1869, 1976.
- Sclater, J.G., R.L. Fisher, P. Patriat, C. Tapscott, and B. Parsons, Eocene to recent development of the South-west Indian Ridge, a consequence of the evolution of the Indian Ocean triple junction, *Geophys. J. R. Astron. Soc.*, **64**, 587-604, 1981.
- Searle, R.C., Lithosphere structure of the Azores plateau from Rayleigh-wave dispersion, *Geophys. J. R. Astron. Soc.*, **44**, 537-546, 1976.
- Shaw, D.M., Trace element fractionation during anatexis, *Geochim. Cosmochim. Acta*, **34**, 237-243, 1970.
- Shibata, T., S.E. DeLong, and D. Walker, Abyssal tholeiites from

- the Oceanographer Fracture Zone. I. Petrology and fractionation, *Contrib. Mineral. Petrol.*, **70**, 89-102, 1979.
- Sigurdsson, H., First-order major element variation in basaltic glasses from the Mid-Atlantic Ridge: 29°N to 73°N, *J. Geophys. Res.*, **86**, 9483-9502, 1981.
- Sleep, N.H. and B.F. Windley, Archean plate tectonics: Constraints and inferences, *J. Geol.*, **90**, 363-379, 1982.
- Stakes, D.S., J.W. Shervais, and C.A. Hopson, The volcanic-tectonic cycle of the FAMOUS and AMAR valleys, Mid-Atlantic Ridge 36°47'N: Evidence from basalt glass and phenocryst compositional variations for a steady state magma chamber beneath the valley midsections, AMAR 3, *J. Geophys. Res.*, **89**, 6995-7028, 1984.
- Stolper, E., A phase diagram for mid-ocean ridge basalts: Preliminary results and implications for petrogenesis, *Contrib. Mineral. Petrol.*, **74**, 13-27, 1980.
- Stroup, J.B., and P.J. Fox, Geologic investigations in the Cayman Trough: Evidence for thin oceanic crust along Mid-Cayman Rise, *J. Geol.*, **89**, 395-420, 1981.
- Sun, S.-S., M. Tatsumoto, and J.-G. Schilling, Mantle plume mixing along the Reykjanes Ridge axis: Lead isotope evidence, *Science*, **190**, 143-147, 1975.
- Takahashi, E., Melting of a dry peridotite KLB-1 up to 14 GPa: Implications on the origin of peridotitic upper mantle, *Tech. Rep. Ser. A*, no. 3, pp. 1-32, Inst. Study of the Earth's Inter., Okayama University, Misasa, Tottori-Ken, Japan, 1985.
- Takahashi, E., and I. Kushiro, Melting of a dry peridotite at high pressures and basalt magma genesis, *Am. Mineral.*, **68**, 859-879, 1983.
- Tamayo Scientific Team: D.G. Gallo, W.S.F. Kidd, P.J. Fox, J.A. Karson, K. Macdonald, K. Crane, P. Choukroune, M. Seguret, R. Moody, and K. Kastens, Tectonics at the intersection of the East Pacific Rise with the Tamayo transform fault, *Mar. Geophys. Res.*, **6**, 159-185, 1984.
- Thompson, G., W.B. Bryan, and W.G. Melson, Geological and geophysical investigation of the Mid-Cayman Rise spreading center: Geochemical variation and petrogenesis of basalt glasses, *J. Geol.*, **88**, 41-55, 1980.
- Verhoogen, J., Petrological evidence on temperature distribution in the mantle of the earth, *Eos Trans. AGU*, **35**, 85-92, 1954.
- Verma, S.P., and J.-G. Schilling, Galapagos hot spot center system, 2, 87Sr/86Sr and large ion lithophile element variations (85°W-101°W), *J. Geophys. Res.*, **87**, 10,838-10,856, 1982.
- Vogt, P.R., Portrait of a plate boundary: The Mid-Atlantic Ridge axis from the equator to Siberia, in *Geology of North America*, vol. M, *The Western North Atlantic Region*, edited by P.R. Vogt and B.E. Tucholke, Plate 8A, Geological Society of America, Boulder, Colo., 1986.
- Walker, D., T. Shibata, and S.E. DeLong, Abyssal tholeiites from the Oceanographer Fracture Zone, II, Phase equilibria and mixing, *Contrib. Mineral. Petrol.*, **70**, 111-125, 1979.
- Watts, A.B., and S.F. Daly, Long wavelength gravity and topography anomalies, *Annu. Rev. Earth Planet. Sci.*, **9**, 415-448, 1981.
- Weaver, J.S., and C.H. Langmuir, Calculation of phase equilibria in mineral-melt systems, *Comput. Geosci.*, in press, 1987.
- Weissel, J.K., and D.E. Hayes, The Australian-Antarctic Discordance: New results and implications, *J. Geophys. Res.*, **79**, 2579-2587, 1974.
- Whitmarsh, R.B., Median valley refraction line, Mid-Atlantic Ridge at 37°N, *Nature*, **246**, 297-298, 1973.
- Zindler, A., and S. Hart, Chemical Geodynamics, *Annu. Rev. Earth Planet. Sci.*, **14**, 493-571, 1986.
- Zindler, A., and E. Jagoutz, Mantle cryptology, *Geochim. Cosmochim. Acta*, in press, 1987.

Emily M. Klein and Charles H. Langmuir, Lamont-Doherty Geological Observatory and Department of Geological Sciences, Columbia University, Palisades, NY 19064

(Received May 6, 1986;
revised March 23, 1987;
accepted March 30, 1987.)